Aging disrupts spatiotemporal coordination in the cycling ovary

Tammy C.T. Lan[1,2,*], David S. Fischer[1,*,†], Alison Kochersberger[3,*], Ruth Raichur[1,*], Sophia Szady[4], Radiana Simeonova[4,5], Andrew Minagar[4,5], Hien Tran[4,5], Alex K. Shalek[1,6,7,8,9], Pardis C. Sabeti[1,10,11,12], Vipin Kumar[1], Giovanni Marrero[1], Irving Barrera[1], Sarah Mangiameli[1], Fei Chen[1,13], Jennifer L. Garrison[3,14-16, †], Hattie Chung[4,17-19, †]

[1]The Broad Institute of MIT and Harvard, Cambridge, MA, USA
[2]Department of Molecular and Cellular Biology, Harvard University, Cambridge, MA, USA
[3]Buck Institute for Research on Aging, Novato, CA, USA
[4]Department of Medicine, Cardiovascular Research Center, Yale School of Medicine, New Haven, CT, USA
[5]Yale College, New Haven, CT, USA
[6]Institute for Medical Engineering and Science (IMES), Massachusetts Institute of Technology, Cambridge, MA, USA
[7]Department of Chemistry, Massachusetts Institute of Technology, Cambridge, MA, USA
[8]Koch Institute for Integrative Cancer Research, Cambridge, MA, USA
[9]Ragon Institute of MGH, MIT and Harvard, Cambridge, MA, USA
[10]Howard Hughes Medical Institute, Chevy Chase, MD, USA
[11]Department of Organismic and Evolutionary Biology, Harvard University, Cambridge, MA, USA
[12]Department of Immunology and Infectious Diseases, Harvard T.H. Chan School of Public Health, Harvard University, Boston, MA, USA
[13]Department of Stem Cell and Regenerative Biology, Harvard University, Cambridge, MA, USA
[14]Center for Healthy Aging in Women, Novato, CA, USA
[15]Department of Cellular and Molecular Pharmacology, University of California, San Francisco, CA, USA
[16]Leonard Davis School of Gerontology, University of Southern California, Los Angeles, CA, USA
[17]Department of Molecular, Cellular and Developmental Biology, Yale University, New Haven, CT, USA
[18]Department of Obstetrics, Gynecology and Reproductive Sciences, Yale School of Medicine, New Haven, CT, USA
[19]Yale Center for Research on Aging, Yale School of Medicine, New Haven, CT, USA
*These authors contributed equally to this work.
[†]To whom correspondence should be addressed: hattie.chung@yale.edu (HC), jgarrison@buckinstitute.org (JG), or david.fischer@meduniwien.ac.at (DSF)

Summary

Throughout the female reproductive lifespan, the ovary completes hundreds of cycles of follicle development, ovulation, and tissue regeneration[1–3]. These processes rely on the precise coordination of intricate multicellular interactions across time and space[4]. How aging disrupts these interactions, leading to the overall decline in reproductive and endocrine functions, remains understudied. To understand the multicellular dynamics that underlie ovarian function and their changes with age, here we use Slide-seq, a near-cellular spatial transcriptomics method, to profile 21 ovaries across reproductive cycles and chronological age, representing 601,831 near-cellular spots across 68 spatial transcriptomic profiles[5,6]. We develop a segmentation analysis to identify static snapshots of spatial niches that capture folliculogenesis *in situ*, allowing us to examine the multicellular dynamics of 345 oocytes, 653 follicles, and 234 corpora lutea. We find that aging disrupts both the spatial organization and temporal coordination of folliculogenesis before the cessation of cycling, leading to dysregulation of hormone production and signaling. These disruptions are marked by altered immune cell dynamics, inflammatory signaling, and global tissue disorganization that impair the cyclic remodeling required for ovarian function. Our findings reveal how multicellular niches orchestrate the reproductive and endocrine functions of the ovary and demonstrate how age-related breakdown of tissue organization across time and space precedes reproductive decline.

48 **Main Text**

49 The ovary is a dynamic organ comprising diverse cell types that undergo continuous remodeling to regulate
50 reproductive and endocrine function throughout the female lifespan. During the female reproductive period, ovarian
51 cells undergo a repetitive cycle of phenotypic switching to collectively orchestrate oocyte maturation, ovulation,
52 and hormone production throughout the estrous or menstrual cycle[4,7]. This process of "homeostatic cycling" occurs
53 approximately 150–650 times in mice and 300–400 times in humans over the course of the female reproductive
54 lifespan[1,2]. During chronological aging, overall reproductive function declines and culminates in the cessation of
55 cycling. Here, we investigate the molecular interactions underlying this process, including the progressive depletion
56 of the ovarian reserve, the decline in the precision of cellular interactions, and the increase in tissue-wide
57 inflammation and fibrosis[8–13].

58

59 Central to ovarian function are spatially organized dynamic multicellular structures – primarily follicles, which
60 develop in distinct stages before transforming into corpora (CL) lutea after ovulation. Folliculogenesis begins with
61 a primordial follicle consisting of a dormant oocyte encased by flattened granulosa cells (GCs). Activation, the
62 awakening of the follicle from its dormant phase, triggers GCs to adopt a cuboidal shape and begin proliferation,
63 forming the preantral follicle where they coordinate morphological and functional changes to support oocyte
64 growth. As the follicle transitions to the antral stage, a fluid-filled cavity (antrum) forms, and the follicle becomes
65 gonadotropin-dependent for growth and begins producing steroid hormones[14,15]. Spatial complexity further
66 increases as theca cells create an outer layer and respond to gonadotropin hormones by producing steroids[16,17].
67 Ultimately, less than 1% of follicles recruited to grow successfully progress to ovulation[18], while the remainder
68 undergo atresia, a form of apoptosis[18]. Though atresia claims most follicles during their maturation process – which
69 spans approximately two weeks in mice and more than a year in humans – the dominant surviving follicle releases
70 a mature oocyte at ovulation. After oocyte ejection, the remaining follicular cells transform into the CL, a transient
71 hormone-producing structure essential for pregnancy and critical in regulating the complex cycle of ovulation[15,19].
72 This creates an extraordinarily complex tissue environment where, at any given time, dozens (mice) or thousands
73 (humans) of follicles at different developmental stages share the same physical space with multiple CLs. The
74 molecular mechanisms coordinating this intricate asynchronous spatiotemporal organization remain unclear,
75 highlighting the need for spatially resolved profiling to better understand the dynamics of these cellular ecosystems.

76

77 Understanding ovarian aging requires studying the interplay between oocytes and their surrounding cells, but
78 current tools are limited in their ability to capture the complexity of these interactions. Previous studies of ovarian
79 aging focused primarily on follicle depletion and decline in oocyte-intrinsic properties such as aneuploidy[20,21].
80 However, mounting evidence suggests that dysfunction across the entire ovarian tissue environment contributes
81 significantly to reproductive aging through dysregulation of these multicellular ecosystems[12,21–23], particularly
82 through disruptions in granulosa cell signaling[24–26], extracellular matrix remodeling[27–30], and immune
83 infiltration[12,31–33], underscoring the need to investigate how multicellular dysregulation drives ovarian aging. Single-

84 cell RNA sequencing is a powerful tool to profile cellular heterogeneity and uncover novel regulatory mechanisms,
85 but it faces limitations in studying ovarian tissue. Droplet-based single-cell methods are limited in their ability to
86 profile large cells like oocytes, which exceed 100 µm in diameter[34–37] and do not resolve interacting cell types in
87 the follicular niche, while coarse spatial transcriptomics approaches lack the resolution to characterize follicular
88 architecture[23,38] and often rely on predetermined gene panels that constrain discovery of novel regulatory patterns
89 within and across niches[39].
90
91 Here we present a spatiotemporal atlas of the cycling murine ovary across chronological aging at near-single cell
92 resolution using Slide-seq[5,6]. Our study comprises *n*=601,831 spots at 10 µm resolution spanning 68 spatial
93 transcriptomic profiles from 21 biological samples collected during the estrus and metestrus stages of the estrous
94 cycle, across three age groups. By developing a segmentation pipeline that specifically captures multicellular
95 structures of the ovary, we identified 345 oocytes, 653 follicles, and 234 CLs, enabling detailed analysis of
96 folliculogenesis and CL dynamics. Comparing profiles between young and aged mice revealed that aging disrupts
97 temporal dynamics of hormone-responsive and hormone-producing processes during the estrous cycle. This
98 disruption coincides with inflammatory processes, global tissue disorganization, and altered dynamics of cyclical
99 remodeling essential for maintaining ovarian function. Our work demonstrates how multicellular niches cooperate
100 to regulate both reproductive and endocrine functions of the ovary and how these interactions become dysregulated
101 with age.
102
103 ***Spatial transcriptomics reveals multicellular organization of the cycling and aging ovary***
104 We used Slide-seq to generate 68 spatial transcriptomics profiles from 21 mice harvested during ovulatory (estrus)
105 and post-ovulatory (metestrus) stages across three age groups, young (10-12 weeks), reproductively middle aged
106 (36-40 weeks), and reproductively old (52-54 weeks)[40] (**Fig. 1a**; **Extended Table 1, 2**; **Methods**). This design
107 enabled us to examine the dramatic post-ovulatory tissue-wide remodeling across the aging trajectory. Unsupervised
108 clustering and *post hoc* annotation of 601,831 high-quality 10 µm spot transcriptomes identified all major ovarian
109 cell types, including oocytes (*Gdf9*), multiple granulosa cell (GC) subtypes, two distinct luteal cell populations,
110 theca cells (*Col1a2*), epithelial cells (*Epcam*), fibroblasts (*Pdgfra*), muscle (*Tagln*), immune (*Lyz2*), endothelial
111 (*Flt1*), and stromal cells (*Aldh1a1*), and others (**Fig. 1b**; **Extended Table 3**). Spatially visualizing cell types revealed
112 spot-level patterns corresponding to the expected histological and morphological organization of the parenchyma,
113 with diverse GCs forming a follicle around an oocyte (**Fig. 1c**).
114
115 To analyze anatomically related groups of spots representing meaningful tissue units, we developed a segmentation
116 pipeline that identified oocytes, follicles, and corpora lutea (CL). As large oocytes often exceed 70 µm in diameter[41],
117 thereby spanning multiple Slide-seq spots, we clustered spatially adjacent putative oocyte spots into segments to
118 create composite oocyte expression profiles for further analysis (**Methods**). In contrast, oocytes in primordial
119 follicles typically span a single spot, which we identified through a separate segmentation pipeline. Spots labeled

120 as 'Oocyte' or expressing *Sohlh1* that were not already assigned to oocyte segments were used to build spatial
121 neighborhood graphs, and segments composed of 2 or more spots with at least one spot expressing *Sohlh1* were
122 assigned as primordial oocytes (**Methods**). We segmented larger structures, including developing follicles and CL,
123 using unsupervised clustering of the spatial neighborhood graph (**Fig. 1d,** left; **Methods**).
124
125 Altogether, we identified 345 oocytes, 653 follicles, and 234 CL *in situ* (**Fig. 1d,** right). Classification of follicle
126 and CL segments based on their GC and luteal composition revealed distinct stages of follicular development,
127 including preantral (N=238), antral mitotic (N=191), antral luteinizing (N=43), and atretic (N=181) follicles, as well
128 as early (N=87) and late (N=147) CL states (**Extended Data Fig. 1a,b; Methods**). Follicle classifications captured
129 the progression of GC function that drives folliculogenesis (**Fig. 1e**), supported by stage-specific expression of key
130 hormone receptors including the anti-Müllerian hormone receptor *Amhr2* in gonadotropin-independent preantral
131 follicles[31] and *Fshr* and *Lhcgr* in gonadotropin-dependent antral follicles[42,43] (**Fig. 1f**). Notably, we identified two
132 distinct luteal cell types that were spatially segregated across two types of CL regulating opposing aspects of
133 progesterone levels[44], the early luteal cells (*Parm1*) promoting progesterone synthesis and late luteal cells (*Akr1c18*)
134 that actively metabolize it (**Fig. 1c,** left, **Fig. 1f; Extended Data Fig. 1c**). These luteal types were labeled 'early'
135 and 'late' according to their temporal function in progesterone regulation throughout the estrous cycle[44].
136 Interestingly, these marker genes of early and late luteal cells corresponded to those previously reported to reflect
137 their presumed cell of origin based on size[45,46], i.e. small luteal cells from theca cells and large luteal cells from
138 GCs[47]. However, our spatially resolved data revealed that these two types generally did not co-localize within the
139 same CL structure (**Extended Data Fig. 1c**), suggesting that this transcriptomic diversity of luteal cells is temporally
140 driven by phenotypic switching, rather than pre-determined by cell-of-origin.
141
142 ***Oocytes follow coordinated transcriptional programs during follicular development***
143 Despite the traditional characterization of oocytes as transcriptionally silent maternal RNA storage units[48], recent
144 studies demonstrate active transcriptional regulation during their maturation[41,49–51]. During each cycle, a subset of
145 primordial oocytes is activated to grow approximately 7-fold in size, progressing from prophase I to arrested
146 metaphase II[52]. We examined the average expression profiles of oocyte segments in their native tissue context,
147 identifying stage-specific expression patterns[34,53–55] defined by their enclosing follicle type, with elevated expression
148 of *Sohlh1* in primordial oocytes[56], *Figla* and *Kit* in preantral follicles, and *Gdf9* and *H1f8* in antral follicles (**Fig.
149 1g**). We next identified distinct gene programs that differ across oocyte maturation by using nonnegative matrix
150 factorization (**Fig. 1h**; **Methods; Extended Data Fig. 1d-f**). Oocyte program 2, characterized by zona pellucida
151 glycoproteins *Zp2* and *Zp3*, indicates upregulation of extracellular matrix components necessary for follicular
152 assembly immediately after primordial follicle activation[47,57]. Oocyte program 4, enriched in F-box proteins
153 (*Fbxw19, Fbxw21, Fbxw24*) that are critical components of the SCF ubiquitin E3 ligase complex controlling cell
154 cycle progression[58,59], emerges in maturing *Bmp15*+ oocytes, reflecting the dynamic transcriptional shifts necessary
155 for meiotic progression. Oocyte program 0 which contains the regulator of meiosis resumption, *Bcl2l10*, and early

156 embryonic development genes *Btg4* and *Tcl1* is upregulated in mature follicles preparing to respond to the
157 gonadotropin surge (**Extended Data Fig. 1e**; $P<0.0001$ preantral vs antral; t-test)[60–62]. Altogether, our findings
158 reveal that oocytes undergo dynamic transcriptional regulation throughout folliculogenesis, switching from
159 processes required to maintain oocyte dormancy to proliferative programs upon follicle activation.
160
161 ***Spatial organization of granulosa cells (GCs) balances proliferation and differentiation***
162 We next investigated how GC states are maintained within follicles throughout folliculogenesis. To systematically
163 compare the spatial organization of GCs across follicles, we devised an analysis to quantify changes in GC
164 characteristics as a function of their scaled radial distance from their follicular center (**Extended Data Fig. 2a**;
165 **Methods**). First, we observed that luteinizing and atretic GCs were most frequently localized to the outer edge of
166 the follicle (**Fig. 1c**). To quantify how this spatial organization emerges during folliculogenesis, we reconstructed a
167 stereotypical differentiation trajectory for GCs using diffusion pseudotime[63] (dpt), based on the coexistence of
168 diverse follicle states captured by our static tissue snapshots (**Extended Data Fig. 2b, c; Methods**). This trajectory
169 captured their maturation paths toward either luteinization or atresia (**Fig. 1e**). Examining GC states in space
170 revealed a striking pattern: GCs at the follicular edge exhibited a non-proliferative state (based on cell cycle scores)
171 and were more differentiated (higher dpt), whereas inner GCs were highly proliferative and less mature, suggesting
172 that follicles grow from the inside out (**Fig. 2a-c; Methods**)[64].
173
174 To uncover the molecular features underlying the spatial organization of follicular function, we applied non-
175 negative matrix factorization (NMF)[65] to identify GC gene programs and analyzed their spatial usage distribution
176 within follicle segments. We found, among others, two key programs related to hormone sensing and production
177 (**Extended Data Fig. 2d-f**; **Methods**). In non-atretic antral follicles, the FSH-regulating program (*Inhbb*, *Inhba*,
178 *Inha*, *Fst*)[43,66] was significantly more active toward the follicular center while the steroidogenesis program
179 (*Cyp19a1*, *Hsd3b1*, *Lhcgr*, *Prlr*)[15,43] was enriched at the follicular edge, where GCs interface with androgen-
180 producing theca cells required for estrogen biosynthesis (**Fig. 2d**, purple lines; Spearman ρ, $*P<0.05$). However,
181 atretic follicles deviate from this spatial pattern, showing reduced FSH program activity at the center and uniformly
182 low steroidogenesis expression throughout the follicle (**Fig. 2d**, orange lines). We thus propose that this spatial
183 compartmentalization establishes a division of labor, with GCs closer to the oocyte initially sensing FSH to regulate
184 oocyte activation and follicle growth, while peripheral GCs synthesize hormones in coordination with theca cells.
185 In atretic follicles, this coordination appears to break down, suggesting a loss of spatially guided functional
186 organization during follicular atresia.
187
188 ***Multicellular dynamics drive folliculogenesis progression***
189 To understand how multiple cell types coordinate during follicle development, we ordered follicle segments along
190 a computationally inferred folliculogenesis trajectory in reproductively young mice. Using the core cell types of
191 follicles, namely oocytes, granulosa, and theca cells, we computed the distributional pairwise distance between all

192 segments using the Wasserstein distance[67] (**Fig. 2e**). We then used this representation of segment dissimilarity to
193 cluster follicles and corpora lutea and computed their UMAP embedding (**Fig. 2f**; **Methods**). To interpolate
194 folliculogenesis events based on this representation, we computed a diffusion pseudotime across follicles, which
195 revealed the expected sequential trajectory from preantral to antral follicles, or atretic follicles (**Fig. 2g**). Analyzing
196 cell type composition along this trajectory highlighted gradual shifts in cell type composition (**Fig. 2i**). While the
197 total proportion of immune cells remained stable across follicle types, their spatial distribution varied significantly,
198 showing increased infiltration near the center of atretic follicles; this observation held true even after accounting for
199 variations in slicing by limiting analyses to follicles containing an oocyte, ensuring that sections captured the follicle
200 center (**Fig. 2j**; $P<0.001$ antral *vs* atretic follicles; Tukey's test, **Extended Data Fig. 2g**). In contrast, the spatial
201 distribution of endothelial cells was indistinguishable across follicle types (**Extended Data Fig. 2h**). The
202 observation that immune infiltration is specific to atretic follicles validates our classification of atretic follicles
203 based on GC expression, which has lacked supporting evidence[35], and aligns with prior observations that immune
204 cells infiltrate dying follicles for tissue clearance[12]. Altogether, our results show that folliculogenesis can be
205 recovered from spatial snapshots of ovarian tissue slices, and that the follicular niche exhibits complex spatial
206 coordination of multicellular patterns along the folliculogenesis trajectory.
207
208 ***Cell-cell interactions drive follicle maturation***
209 Based on our observations that follicles undergo significant compositional changes across folliculogenesis, we next
210 sought to understand molecular interactions that mediate changes in cell-cell communication within each follicular
211 type. To investigate interactions between cell types regulating folliculogenesis, we used MultiNicheNet[68] to analyze
212 receptor-ligand pairs among oocytes, granulosa (GC), theca, and immune cells across preantral, antral, and atretic
213 follicles, treating each follicle as a sample (**Methods; Extended Data Fig. 2i**). Interactions specific to each follicle
214 type included *Gdf9-Fxyd6* between oocytes and GCs in preantral follicles, *Fst-Bmpr1b* between GCs and theca cells
215 in antral follicles, and *Apoa4-Lrp1* within GCs in atretic follicles. Scores for these interactions varied smoothly
216 across the folliculogenesis trajectory (**Fig. 2k, Methods**). The candidate atretic interaction, *Apoa4-Lrp1*, suggests
217 a role for metabolic shifts within the follicle, as *Lrp1* (low-density lipoprotein receptor-related protein 1) regulates
218 lipid transport, glucose metabolism, and energy homeostasis[69–71], while *Apoa4* promotes lipid transport and
219 metabolism, and their interaction facilitates glucose uptake[72]. Notably, a recent genome-wide association study
220 linked *LRP1* with polycystic ovarian syndrome (PCOS), an ovarian disorder characterized by metabolic and
221 hormonal dysfunction[72].
222
223 ***Temporal variation in follicle activation, maturation, and hormone sensing***
224 Although all follicles in the ovary experience the same systemic hormone environment, diverse follicle states coexist
225 across the estrous cycle in young mice. In reproductively young animals, we found fewer preantral follicles in
226 metestrus than in estrus, suggesting that a new pool of preantral follicles may develop into a gonadotropin-
227 independent state right after ovulation (**Fig. 3a**; $P=0.001$, two-tailed t-test). We next compared characteristics of

228 antral follicles between the estrus and metestrus stages to further understand how gonadotropins affect follicle states
229 across the cycle in reproductively young mice. Immediately before estrus, a surge in follicle-stimulating hormone
230 (FSH) and luteinizing hormone (LH) initiates competition among antral follicles for dominance, leading them to
231 either ovulation or atresia, such that mature antral follicles are typically absent by estrus[73]. Consistently, within
232 reproductively young mice we observed significantly smaller antral mitotic follicles in estrus than in metestrus
233 (**Extended Data Fig. 3a;** P=0.001, two-tailed t-test). Follicles in estrus overall exhibited a lower average
234 pseudotime, suggesting a less mature follicle state (**Fig. 3b**; **Extended Data Fig. 3c;** P=0.002, two-tailed t-test).
235 Functionally, all antral follicles at estrus showed significantly lower expression of the gonadotropin receptors *Lhcgr*
236 and *Fshr* (**Fig. 3c**; *P<0.01, **P<0.001, two-tailed t-test), implying that antral follicles at estrus are in an immature
237 and non-hormone-responsive state, possibly due to their recent transition from the gonadotropin-independent
238 preantral state[14].
239
240 ***Aging disrupts homeostatic folliculogenesis***
241 A hallmark of ovarian aging is the onset of irregular cycling, as observed during perimenopause in humans,
242 indicating disrupted temporal regulation of endocrine signaling and ovarian function[74,75]. Although we confirmed
243 that reproductively old mice in our study were cycling at the time of tissue harvest, we investigated whether our
244 molecular measurements in these mice exhibited signs of temporal dysregulation and loss of the homeostatic
245 features that we identified in young mice. First, in old mice, we no longer found evidence of a shift in the
246 composition of preantral follicles nor the sizes of antral follicles across stages (**Fig. 3d**; P=0.942, two-tailed t-test;
247 **Extended Data Fig. 3b**). To compare follicle dynamics across estrus and metestrus in aged ovaries, we projected
248 follicles from old mice into the reference trajectory of young mice, again using the distributional distance
249 (**Methods**), and used this projection to assign pseudotime to follicles in old mice. In old mice, the distribution of
250 this pseudotime was distorted, showing no significant distinction between estrus and metestrus (**Fig. 3e**; P=0.677,
251 two-tailed t-test; **Extended Data Fig. 3c**). Furthermore, *Fshr* and *Lhcgr* expression within all antral follicle types
252 did not differ across estrus and metestrus in old mice, unlike in young mice (**Fig. 3f**). These findings suggest that
253 the decoupling of folliculogenesis, estrous cycle, and follicular hormone sensing occurs with age and precedes the
254 cessation of cycling.
255
256 Aging leads to both depletion and dysfunction of maturing oocytes across follicle stages (**Fig. 3g**). The quality of
257 oocytes decreases with age, in part due to dysregulation of the follicle niche[76–78]. To understand how oocytes are
258 affected by this dysregulation, we performed differential expression analysis in maturing oocytes of young and old
259 animals and identified a set of genes that undergo monotonic changes across aging (**Fig. 3h, Extended Data Fig.
260 3d; Methods**). In particular, the expression of the nuclear androgen receptor *Ar* and hydroxysteroid dehydrogenase
261 *Akr1c18,* known to metabolize progesterone, increased in aging oocytes. These genes are known to be involved in
262 oocyte maturation and meiosis progression[79,80], and their upregulation may reflect an adaptive shift by oocytes to
263 changing hormone levels in the aging ovarian environment[68]. Furthermore, we observed decreased expression of

264 the insulin-degrading enzyme *Ide*, which attenuates insulin signaling in healthy folliculogenesis[69,70]. Insulin
265 signaling regulates the final stages of oocyte maturation, although high insulin levels can reduce oocyte quality,
266 underscoring the need for balanced signaling[81,82]. Interestingly, aging oocytes show dysregulation of the *Nlrp9b*
267 family genes (*Nlrp9a/b/c*), which normally increases during late maturation in young oocytes[83] (**Extended Data**
268 **Fig. 3e**). These NOD-like receptor homologs localize to the subcortical maternal complex and are thought to
269 regulate the oocyte-to-embryo transition[82,84], though their role is under debate[84]. Together, our results demonstrate
270 that aging disrupts the integration of external signals that guide oocyte maturation, suggesting a potential
271 mechanistic basis for age-related decline in oocyte quality.
272
273 ***Temporal dysregulation of corpus luteum (CL) clearance in aged ovaries***
274 We found that aging not only impacted folliculogenesis towards ovulation, but also significantly altered the
275 dynamics of CL progression. Young ovaries maintained a distinct temporal pattern of dominating presence of early
276 CLs at estrus and late CLs at metestrus, which supports the synthesis and upregulation of progesterone in the luteal
277 phase immediately after ovulation, followed by a timely decrease in progesterone levels to allow the next cycle to
278 progress. By contrast, the estrus stage of aged ovaries exhibited an accumulation of late CLs, which metabolize
279 progesterone (**Fig. 3i**, P=0.006, two-tailed t-test). We hypothesize that this accumulation would disrupt the
280 regulation of progesterone levels, potentially impacting the hormonal response of future cycles[4,14].
281
282 We leveraged our spatial data to understand how CLs interact with their tissue environment during the estrous cycle
283 and found that during their homeostatic progression, late CLs recruit immune cells required for tissue clearance
284 during luteolysis[12] (**Fig. 3j**). We examined immune infiltration across CL types by age and stage, which revealed
285 their significant accumulation in late CLs in the metestrus stage of old ovaries (**Fig. 3k; Extended Data Fig. 3f;**
286 P<0.005, two-tailed t-test), supporting the hypothesis that the failure to clear late CLs from the preceding cycle
287 leads to chronic immune recruitment[85]. Further supporting this observation, aged ovaries exhibited downregulation
288 of the luteolysis-triggering prostaglandin receptor *Ptgfr,* essential for CL breakdown (**Fig. 3l;** P=0.03, two tailed t-
289 test) and increased expression of immune-recruiting chemokine *Ccl2*, along with pro-inflammatory cytokines *Il1b,*
290 *Ccl3,* and *Tnf*[31,36,37] (**Fig. 3l**). Altogether, our findings show that impaired clearance of late CLs contributes to
291 chronic immune recruitment, inflammation, and declining endocrine function with age.
292
293 In summary, we observe that aging disrupts the temporal coordination between spatial niches of the ovary and their
294 response to external regulatory cues. In young ovaries, gonadotropins pace growing follicle cohorts, ensuring
295 appropriate progression towards ovulation or atresia, with immature follicles emerging at estrus. In old animals,
296 this pacing becomes dysregulated, with larger and more mature follicles present in estrus (**Fig. 3m**). Similarly, aged
297 CLs exhibit decreased expression for prolactin and prostaglandin receptors, cueing regression, which may delay
298 regression and increase immune cell recruitment (**Fig. 3n**).
299

300 ***Global inflammatory changes mark ovarian aging***

301 Ovarian aging is marked by a global change in tissue function, including increased inflammation, which may
302 broadly disrupt tissue homeostasis[11,86]. To examine how aging alters the stroma that may contribute to this decline,
303 we analyzed age-related changes in stromal cell composition and function. Compositional analysis revealed an age-
304 associated increase in surface epithelium and immune cells, alongside a reduction in steroidogenic stromal cells,
305 occurring monotonically over young, reproductively middle-aged, and old mice[86–89] (**Fig. 4a;** compositional test
306 with scCODA[90]; **Extended Data Fig. 4a**; **Methods**). This shift coincided with significant changes in several
307 molecular signatures, including reduced extracellular matrix deposition genes, increased metalloproteases required
308 for tissue remodeling, increased fibrosis, and increased inflammation[86] (**Fig. 4b; Extended Data Fig. 4b**). To
309 further understand the spatial maintenance of inflammation, we analyzed immune gene program usage across spatial
310 compartments and found two programs of note, program 2 (*Cd74* and *Ccl22*) that suggested a possible role in wound
311 healing[87–89,91], and program 3, characterized by pro-inflammatory markers *Lyz2* (lysozyme 2), *Gpnmb* (glycoprotein
312 NMB), and *Lgals3* (galactin-3)[92–97] (**Methods; Extended Data Fig. 4c**). While the expression of immune program
313 2 did not change with age (**Fig. 4c**; $P>0.05$ (ns), two-tailed t-test), immune program 3 was upregulated across all
314 spatial compartments in older mice (**Fig. 4c**; ***$P<0.0005$, t-test), suggesting that inflammatory processes are
315 globally upregulated with aging.

316

317 A defining feature of the aging ovary is the accumulation of multinucleated giant cells (MNGCs), derived from
318 macrophage fusion in the stroma, which reflects global inflammation and is associated with fibrosis[11,31,98,99]. We
319 observed MNGCs in our histological analysis of adjacent sections accompanying each Slide-seq tile, visible as
320 masses of cellular fusion events on hematoxylin and eosin (H&E) stains, whose presence increased with age (**Fig.
321 4d,e**). To identify the transcriptomic features of MNGCs, we conducted image registration between adjacent pairs
322 of H&E images and Slide-seq puck using manually selected anatomic hallmarks, then segmented MNGCs (**Fig. 4f;
323 Methods; Extended Data Fig. 4e**). This segmentation allowed us to stratify immune cells that lie within *vs* outside
324 of MNGCs, which we then leveraged to identify differentially expressed genes between those two compartments of
325 the ovarian stroma. Immune spots in MNGCs showed significant upregulation of *Fth1, Lyz2, Gpnmb, Ctsd, Lgals3*
326 (**Fig. 4g**). Notably, these genes coincide with immune program 3, whose expression is highly elevated across all
327 spatial compartments, thereby suggesting a possible link between the accumulation of tissue-wide inflammatory
328 processes and those in MNGCs. Taken together, these changes indicate a decreased ability of immune cells to
329 maintain homeostasis during the cyclical remodeling that occurs within the stromal compartment of the ovary,
330 instead compounding inflammation and fibrosis.

331

332 ***A model for global tissue disorganization in ovarian aging***

333 We hypothesized that multicellular changes in the ovarian stroma during aging collectively disrupt coordination
334 between follicles. To test this, we analyzed the spatial organization of entire niches by assessing the co-localization
335 of homotypic follicles. At smaller length scales (neighborhood radius <500 μm), both preantral and atretic follicles

336 were highly co-localized amongst themselves in young but not in aged mice (**Fig. 4h; Methods**). These findings
337 align with prior studies highlighting the importance of follicle crowding, particularly during early follicle activation
338 and among preantral follicles[100,101]. Decreased preantral clustering with age is hypothesized to result in part due to
339 the increased rigidity of the ovarian extracellular matrix[51,86]. The observed co-localization of atretic follicles in
340 young mice suggests a role for spatially regulated paracrine signaling during follicle selection, potentially mediated
341 by the dominant follicle. In contrast, antral follicles did not co-localize at small length scales in either young or old
342 mice, supporting the hypothesis that dominant follicles act as isolated "islands" during follicle selection. However,
343 the co-localization of antral follicles at larger spatial scales (neighborhood radius > 2000 μm) in both young and
344 old mice may simply reflect the overall larger size of the ovary in young mice (~3000 μm in total diameter). These
345 results highlight the changing landscape of follicular crowding and global tissue organization with aging, in
346 particular, the decreased density of preantral follicles that may impact interfollicular communication and
347 coordinated follicular dynamics.
348
349 The loss of global spatial organization in aged ovaries suggests that inflammatory changes disrupt both individual
350 follicle function and their coordinated development, thereby indicating molecular hallmarks of ovarian aging at the
351 level of cells, niches and the full tissue (**Fig. 4j**). At the level of the oocyte, reproductive function is impaired as the
352 total number of maturing oocytes per tissue declines and the gene expression state of the remaining oocytes changes
353 with age. These changes in oocytes interact with alterations in their surrounding niches: within individual follicles,
354 inflammatory gene expression shifts, and entire niches become less responsive to the estrous cycle. This is
355 demonstrated by the fraction of preantral follicles that no longer vary with stage in old mice and by the accumulation
356 of late CLs in ovaries of old mice due to impaired clearing. Meanwhile, at the level of the organ, the surface
357 epithelium thickens, and the stroma becomes dominated by aberrant inflammation that includes the build-up of
358 MNGCs. In summary, age-related inflammation progressively compromises tissue organization and remodeling
359 across multiple spatial scales, from cellular composition to multicellular structure arrangements.
360
361 **Discussion**
362 Using spatial transcriptomics with near cellular spot resolution, we analyzed 310 oocytes, 653 total follicles, and
363 234 corpora lutea (CL) in their native tissue context to reveal fundamental principles of ovarian tissue organization
364 and their age-related dysregulation. We used spatially contextualized gene expression profiles to map out transitions
365 of entire spatial niches during folliculogenesis, leveraging static tissue snapshots that capture asynchronous stages
366 of a dynamic process. Our findings highlight the governing principles of homeostatic remodeling of the ovary driven
367 by temporally fluctuating hormone functions of granulosa cells (GCs), changes in cell-cell communication between
368 the oocyte and its surrounding cells, and hormonal features of entire follicles. By examining entire multicellular
369 structures rather than isolated cells, we uncovered key principles of ovarian organization: radial specialization
370 within follicles, local coordination between neighboring structures, and tissue-wide patterns of immune function
371 that become dysregulated with age.

The spatial organization of GCs within follicles represents an elegant solution to competing metabolic demands. By segregating proliferative activity to inner GCs while outer cells specialize in hormone sensing and production, follicles can simultaneously maintain growth while developing distinct endocrine functions[64,102]. As hormone signaling and production are energy and resource-intensive processes, it may be advantageous to limit these functions to a subset of cells within follicles. Localizing GC hormone functions to the follicle edge likely promotes rapid signaling exchange with the vasculature and stroma, enabling swift endocrine responses critical for follicular maturation. This spatial arrangement allows peripheral GCs to differentiate and support steroidogenesis without compromising the proliferative capacity of less mature, inner GCs. Furthermore, this radial organization of hormone signaling components suggests a potential mechanism for signal propagation via a gradient from the follicular periphery to the oocyte to coordinate maturation, and that dysregulation in such spatial coordination of GCs may contribute to atresia. Our observations identify multiple features of atresia: atretic signals are at the outer edge of the follicles, the spatial division of labor between hormone sensing and synthesis in GCs is lost, and immune cells infiltrate follicles. However, cues of and trajectories to atresia are not yet fully elucidated[17,103–105].

Our findings reshape our understanding of temporal coordination in ovarian function. While the ovulation cycle is often viewed primarily as a mechanism for oocyte release, our results highlight the extensive tissue-wide remodeling of the entire ovary required for successful cycling. The precise temporal patterns we observed in young mice, from follicle activation to CL clearance, suggest that local tissue organization plays a crucial role in cycle progression. For example, global neuroendocrine signals governing follicle selection synchronize the development of antral follicles within specific temporal windows of the estrous cycle. The breakdown of this temporal coordination with age, even before cycle cessation, indicates that spatial organization and temporal progression are intricately linked. We note that these multicellular features of reproductive function in young mice and their progressive dysfunction in old mice are exceptionally dynamic with an estrous cycle length of only four days. On this time scale, spatial transcriptomics is a useful method to capture snapshots of meaningful niche transitions and has allowed us here to describe changes across scales, from radial heterogeneity within follicles, to variation across follicles, and spatial patterns of follicle co-localization that underscore the importance of interfollicular coordination.

The age-related changes we observed suggest a model where disruption of tissue organization triggers a cascade of dysfunction. The extended presence of late CLs that fail to clear from the prior cycle may also contribute to the age-related decline in systemic progesterone levels[106]. Failed clearance of CL appears to trigger chronic immune recruitment, evidenced by elevated levels of *Ccl2* expression in the luteal cells of the aged ovary, while the emergence of multinucleated giant cells signals a shift from homeostatic to inflammatory immune function. The loss of spatial correlation between neighboring follicles suggests that age-related stromal changes disrupt extracellular matrix remodeling and paracrine signaling necessary for coordinated development. These changes precede the end of cycling, suggesting they may represent early events in reproductive aging.

These results have potential implications for understanding and mitigating human reproductive aging, which remains challenging to profile at scale and high temporal resolution. The observation that spatial and temporal coordination break down before cycle cessation suggests new approaches for detecting and potentially intervening in age-related fertility decline. Additionally, the role of tissue-wide organization in maintaining function suggests that therapeutic strategies may need to target the entire ovarian environment rather than focusing solely on oocytes or follicles.

Several key questions emerge from our findings. First, how do GCs maintain distinct functional zones despite their high proliferation rate? Second, what signals coordinate states between neighboring follicles? Understanding these mechanisms could reveal new principles of tissue organization. Third, where do regressed CLs go? Fourth, how does the relationship between immune function and tissue organization change during aging? Immune cells play critical functions in maintaining tissue homeostasis in the ovary, particularly during the clearance of atretic follicles and regressing CLs[107]. Aging disrupts the homeostatic tissue remodeling that governs the organ-intrinsic "clock" regulating ovulatory cycles. Whether interventions targeting inflammatory pathways could preserve ovarian function with age is an open question.

We acknowledge several limitations in our study. While spatial transcriptomics provides unprecedented insights into tissue organization, we lack direct observation of fate decisions, for example pinpointing the exact step in our molecular representation of folliculogenesis at which atresia begins or which follicles contain successfully ovulated oocytes. Future studies combining this approach with lineage tracing could reveal how spatial patterns influence developmental trajectories. Additionally, consistent with previous observations, our studies in C57BL/6 mice showed increased inflammation during aging, but the role of fibrosis remains unclear[108]. We did not observe a decline in the vascularization of CLs in aged ovaries, which may reflect a strain-specific difference as well as the impact of superovulation used in a prior study[109]. Additionally, validation in human tissue will be important for translating these findings into clinical applications.

Here we demonstrate that ovarian function requires precisely coordinated spatial and temporal organization across multiple scales, from cell-type specific patterning within follicles to tissue-wide immune function and that spatial transcriptomics technologies have the chance to capture meaningful multicellular transitions if carefully analyzed, positioning this methodology as a key instrument to derive mechanistic insights into reproductive function. Understanding how this organization fails with age opens new avenues for preserving fertility and ovarian endocrine function.

441 **Figure 1. A spatiotemporal map of the cycling and aging ovary identifies spatial niches driving**
442 **folliculogenesis.**
443 **a.** Overview of experimental design and workflow. Profiling the cycling and aging murine ovary using near-single-
444 cell resolution spatial transcriptomics. Mice were staged using vaginal cytology and harvested at the estrus and
445 metestrus stages, totaling n=21 mice sampled across young (10-12 weeks), middle (36-40 weeks), and old (52-54
446 weeks) age groups. Multiple non-adjacent sections were sampled from each ovary with a minimum gap of 200 µm
447 to reduce resampling of the same follicle or corpus luteum (CL) structure. Tissue sections (10 µm thickness) were
448 profiled with Slide-seq and adjacent sections were taken for histological analysis.
449 **b.** Cell types of the mouse ovary identified by unsupervised clustering of gene expression profiles obtained from
450 Slide-seq spots. UMAP embedding of RNA profiles captured by Slide-seq spots (n=601,831; each at 10 µm
451 resolution) across all 68 Slide-seq pucks (**Methods**). Spots are colored by cluster and post hoc annotation (color
452 legend). "GC": granulosa cell clusters. Right: Mean expression (log normalized counts, dot color) and proportion
453 of expressing cells (dot size) of marker genes (columns) in each group used for annotating cell type clusters (rows).
454 **c.** Spatial projection of cell type labels of spots on a representative Slide-seq puck. Spots corresponding to select
455 cell types that delineate the parenchyma (follicles, CL) are shown; all other cell types are shown in gray. The
456 corresponding adjacent H&E section is shown below. Right: deconstruction of multiple cell types that comprise an
457 example follicle.
458 **d.** Segmentation pipeline for the identification of key morphological and functional structures of the ovary. Left:
459 Large oocyte (pink) transcriptomes sampled across multiple spots were combined to reflect their single-cell origin
460 (dark blue), while presumed primordial oocytes (light blue) were detected using a separate pipeline (**Methods**).
461 Large multicellular segments of follicles and CL were detected by unsupervised clustering on the spatial
462 neighborhood graph of core cell types (pink: oocyte, green: GC, orange: theca, blue: luteal) (**Methods**). Right:
463 Summary of all detected follicle and CL segments.
464 **e.** Schematic overview of folliculogenesis and CL formation. GCs form a single layer around a dormant oocyte in
465 primordial follicles. Activation triggers GCs to proliferate, forming the preantral follicle. The follicle then
466 transitions to the gonadotropin-dependent antral stage during which a fluid-filled cavity forms the antrum. Theca
467 cells are recruited to create an outer layer, and GCs differentiate into multiple subtypes. Follicle atresia can occur
468 during any stage of folliculogenesis. After ovulation, GCs luteinize into luteal cells that form the CL, which is
469 subsequently cleared from the tissue.
470 **f.** Mean expression (log normalized counts and variance-scaled) of key hormone receptors and synthesis genes
471 (columns) across each segment type (rows). Genes are arranged based on their involvement in gonadotropin-
472 independent, gonadotropin-dependent growth, and luteinization.
473 **g.** Mean expression (log normalized counts and variance-scaled) of marker genes (columns) within composite
474 oocytes organized by the enclosing follicle at different stages of folliculogenesis (rows).
475 **h.** Transcriptomic diversity of oocytes measured *in situ*. Left: Principal component (PC) embedding of n=345
476 composite oocyte RNA profiles (dot) indicating the stage of its enclosing follicle (color). Center: Example spatial

477 plots of two pucks showing oocytes (colored dots) in their native tissue context depicting the stage of its enclosing
478 follicle (color), with surrounding GC spots (dark gray). Right: expression (color) of oocyte gene programs identified
479 via non-negative matrix factorization (**Methods**). Top genes contributing to each oocyte gene program, gray text
480 box.

481 **Figure 2. Spatiotemporal coordination within follicular niches across folliculogenesis.**
482 **a.** Top: spatial plot of an example puck showing follicular cell types (colors), including preantral, antral early
483 mitotic, antral mitotic, antral luteinizing, and atretic granulosa cell (GC) subtypes, and oocyte and theca. Bottom:
484 Mean proportion of each GC subtype (colored lines, y axis) within each follicle type (panels) as a function of the
485 relative radial distance from the follicle center (x axis), scaled from 0 (follicle center) to 1 (follicle edge) across 10
486 uniform bins. Shaded lines represent the standard error of the mean (SEM) fraction across follicles within each
487 radial bin. Monotonically significant radial trends are indicated (*P<0.05, Spearman correlation coefficient).
488 **b.** Diffusion pseudotime (dpt) trajectory analysis of GCs. Left: Spatial plot of an example puck showing GC dpt
489 values (colorbar) calculated separately across two follicle fates, non-atretic (purple) and atretic (orange). Right:
490 Mean dpt of GCs (y axis) across the relative radial distance from the follicle center (x axis), scaled from 0 to 1 as
491 before; shaded lines represent the SEM across follicles within each radial bin. Monotonically significant radial
492 trends are indicated (*P<0.05, Spearman correlation coefficient).
493 **c.** Cell cycle analysis of GCs. Left: spatial plot of an example puck showing the cell cycle state (cycling, G2M/S,
494 pink; non-cycling, G1, gray; **Methods**). Right: Mean proportion of GCs in cycling or noncycling state (y axis)
495 across the relative radial distance from the follicle center (x axis), scaled from 0 to 1 as before; shaded lines represent
496 the SEM across follicles within each radial bin. Monotonically significant radial trends are indicated (*P<0.05,
497 Spearman correlation coefficient).
498 **d.** GC gene programs identified by cNMF (**Methods**). Left: Spatial plot of an example puck showing the expression
499 of two distinct programs (colorbar) related to hormone regulation, FSH regulation (top) and steroid hormone
500 synthesis (bottom). Top contributing genes of each program are shown in the gray box. Right: Mean usage score of
501 each program in GCs (y axis) across the relative radial distance from the follicle center (x axis), scaled from 0 to 1
502 as before; shaded lines represent the SEM across follicles within each radial bin. For each program (FSH regulation,
503 top; steroidogenesis, bottom), its radial usage is shown among non-atretic antral follicles (purple) and atretic
504 follicles (orange). Non-atretic follicles: FSH regulation program, Spearman ρ=-0.61, *P<0.05; steroidogenesis
505 program, Spearman ρ=0.91, **P<0.01.
506 **e.** Schematic of inferring multicellular transitions between follicles using optimal transport, by aligning pairs of
507 follicles based on their distributional distance. Pairing of transcriptionally similar cells (e.g. GC to GC) incurs a
508 low distance, while pairing transcriptionally different cells (e.g. theca to GC) incurs a high distance.
509 **f.** Result from optimal transport-based calculation of segment-segment similarity. Left: Pairwise transition matrix
510 between all segments (rows, columns) of young mice showing the transport cost (color, blue gradient) organized
511 by unsupervised hierarchical clustering (dendrogram, axes). Segment type is annotated by their corresponding color
512 in **g**. Right: UMAP embedding of all segments (dots) based on their transport cost matrix, follicles (pale green) and
513 corpora lutea (yellow and purple).
514 **g,h.** Interpolation of the folliculogenesis trajectory. UMAP embedding of follicles only (dots) based on their
515 transport cost matrix, colored by their segment type (**g**) and the inferred folliculogenesis a diffusion pseudotime
516 progression (dpt, colorscale) of each follicle (dot) (**h**).

517 **i.** Cell type composition (colors, y axis) of each follicle (bars, x axis) ordered by their folliculogenesis diffusion
518 pseudotime as in **h**.
519 **j.** Mean proportion of immune cells within follicles (y axis), by follicle type (color, lines), across the relative radial
520 distance from the follicle center (x axis), scaled from 0 to 1 as before; shaded lines represent the SEM across
521 follicles within each radial bin. Comparison of the immune fraction between atretic *vs* aggregated non-atretic
522 follicles, based on the distribution of immune fraction across individual follicles within each radial bin
523 (***$P<0.0005$, Tukey's test; **Methods**).
524 **k.** UMAPs of inferred folliculogenesis trajectory showing mean ligand-receptor expression scores (color) in each
525 follicle (dot), based on significant interactions identified by MultiNicheNet (**Methods**). The ligand (panel title, left)
526 and its corresponding receptor (panel title, right) are colored by the cell type expressing each component (legend).
527

528 **Figure 3. Aging disrupts the temporal variation in folliculogenesis and corpus luteum (CL) clearance.**
529 **a-f.** Follicle characteristics in young (**a-c**) and old mice (**d-f**). **a,d.** Fraction of each follicle type per puck (y axis)
530 across samples from estrus and metestrus (x axis; $^{**}P<0.005$, ns – not significant, two-tailed t test). **b,e.** Boxplot
531 of diffusion pseudotime of follicles (dpt; y axis) by stage (x axis, bar shading) ($^{**}P<0.005$, ns – not significant;
532 two-tailed t-test of means). Center line indicates median, box bounds represent first and third quartiles, whiskers
533 span from each quartile to the minimum or the maximum (1.5 interquartile range below 25% or above 75%
534 quartiles). **c,f.** Mean expression of key hormone receptor genes (x axis) of individual follicles grouped by follicle
535 type (color) and across stages (bar shading). Error bars: SEM of gene expression of individual follicles across
536 follicle types ($^{*}P<0.05$, $^{***}P<0.01$, two-tailed t-test; all other bar groups, not significant).
537 **g.** Total composite oocyte count (y axis) by enclosing follicle type (color) across age groups (x axis).
538 **h.** Differentially expressed genes of oocytes across age. Select genes whose composite expression patterns (y axis)
539 in maturing oocytes (dots) significantly changed across age (color; $^{*}P<0.05$, $^{**}P<0.005$, $^{***}P<0.0005$, two-tailed
540 t-test, Benjamini-Hochberg correction; **Methods**). Significant genes were first identified by comparing young and
541 old oocytes, then tested pairwise between young, middle, and old to identify monotonic trends.
542 **i.** Fraction of each CL type within estrus stage, calculated per puck (y axis) and grouped by age (x axis). Error bars:
543 standard deviation of the CL fraction across pucks.
544 **j.** Composition of major cell types in CL subtypes. Boxplot showing distribution of spot (y axis, $\log_{10}$ scale) core
545 cell types (luteal (early and late combined), immune, vascular; color) across the two types of corpora lutea, CL –
546 early and CL – late ($^{***}P<0.001$, $^{****}P<0.0001$, ns – not significant; two tailed t-test of means). Boxplot elements
547 same as in **b,e**.
548 **k.** Spatial plots of four example pucks, shown across stage (estrus *vs.* metestrus) and age (young *vs.* old). Cell types
549 (color) shown: luteal (blues) and immune (yellow); all other cell types, gray.
550 **l.** Mean expression (log normalized counts, dot color) and proportion of CL - late segments (dot size) expressing
551 selected genes (x-axis) involved in CL clearance and immune cell recruitment, grouped by age and stage (rows).
552 **m.** Schematic overview of age-related changes in folliculogenesis across the estrous cycle. Maturation state of
553 follicles in old and young animals. Relative levels of pituitary gonadotropins FSH (blue) and LH (pink) across
554 estrus stages (diestrus (D), proestrus (P), estrus (E), metestrus (M)), and their corresponding receptor expression in
555 antral follicles.
556 **n.** Schematic overview of age-related changes in CL clearance across the estrous cycle. CL formation, immune
557 recruitment, and clearance in young and old animals. Relative levels of CL-derived progesterone (P4) and CL-
558 maintenance signal prolactin (PRL) across estrus and metestrus.
559

560 **Figure 4. Loss of tissue-wide homeostatic remodeling with aging.**

561 **a.** Compositional changes of select stroma cell types across aging. Left: Proportion (y axis) of each cell type (x axis)
562 for individual pucks (points) and averaged across pucks (bars). Credible and significant changes in composition
563 with age was determined using scCODA using all cell types (**Extended Data Fig. 4a)** with "Epithelial – oviduct"
564 as the reference (**Methods**; black bars). Right: Mean proportion of all other cell types within individual pucks (y
565 bars) across ages (x axis); full distribution shown in **Extended Data Fig. 4a**.

566 **b.** Mean expression (log normalized counts and variance-scaled) of genes differentially expressed across ages
567 involved in extracellular matrix remodeling and inflammation (columns) in stromal cells ("stromal – non-
568 steroidogenic", "stromal – steroidogenic", "fibroblast") across age groups (rows). Genes were identified through
569 differential expression analysis across young and old stromal spots (**Methods**).

570 **c.** Changes in immune gene program usage across spatial niches and age. Mean expression of immune programs 2
571 and 3 (y axis) determined by NMF within immune spots, grouped by segment assignment (x axis) and age (color).
572 Top gene correlates of each program are shown in the gray box. Comparison of program scores in young *vs* old
573 (***P<0.0005, two tailed t-test). Error bars: standard error of mean expression across segments.

574 **d.** Identification of multi-nucleated giant cells (MNGCs) from histology sections. Example of hematoxylin and
575 eosin (H&E) stained section of an aged ovary. Masks were manually drawn around MNGCs (**Methods**).

576 **e.** Distribution of histology sections (y axis) annotated with MNGC content across age groups (x axis). All puck-
577 adjacent histology sections were stained with H&E and manually annotated for MNGC content and labelled as
578 'MNGC high' or 'MNGC low' (**Methods**).

579 **f.** Example registration of MNGC masks from H&E images to Slide-seq spots from adjacent sections using Napari
580 (**Methods**). Slide-seq spots are annotated by their annotated cell type (colors) as described above.

581 **g.** Marker genes of stromal immune cells in old mice that contrast immune cell spots within MNGCs with those
582 outside of MNGCs. Mean expression (log normalized counts, dot color) and proportion of expressing immune cells
583 (dot size) of differentially expressed genes (rows) in MNGCs *vs* stromal (rows). Genes were identified by
584 differential expression analysis (**Methods**).

585 **h.** Spatial neighborhood analysis of co-localization patterns among homotypic follicles. Z-scores of follicle co-
586 localization (y axis) as a function of increasing spatial radius (x axis) on the spatial neighborhood graph, tested
587 across step sizes of 200 μm, compared to the null (z-score 0, black dotted line). Co-localization test was conducted
588 across three follicle types (from top to bottom: preantral, antral, atretic) and within each age group (colors).

589 **i.** Schematic overview of hallmarks of the aging ovary. Aging impacts key processes underlying tissue-wide
590 homeostasis, impacting both the reproductive and endocrine functions of the ovary. In young ovaries (green),
591 temporal regulation of folliculogenesis, spatial domain integrity, immune homeostasis, and healthy stromal
592 remodeling are preserved, supporting proper ovarian function. In contrast, aged ovaries (blue) exhibit loss of
593 temporal regulation, delayed corpus luteum clearance, tissue disorganization, follicle depletion, accumulation of
594 MNGCs, inflammation, fibrosis, and thickened surface epithelium, contributing to functional decline.

595

596 **Extended Data Figure 1. Classification and characteristics of segments driving folliculogenesis.**

597 **a.** Boxplot showing the distribution of spot-level cell type composition (y axis, colors) across segment labels (x
598 axis). Boxplot: center line indicates median, box bounds represent first and third quartiles, whiskers span from each
599 quartile to the minimum or the maximum (1.5 interquartile range below 25% or above 75% quartiles).

600 **b.** Principal component analysis (PCA) of segments based on cell type composition. Left: PCA representation of
601 segments labeled by their assigned type (color). Right: PCA of segments by spot counts.

602 **c.** Spatial visualization of luteal cell markers of an example puck. Top: cluster annotation showing early (light blue)
603 and late (dark blue) luteal cells. Middle and bottom: expression of luteal subtype markers *Parm1* and *Akr1c18*
604 shown as normalized expression values (blue intensity scale bars, right). All other cell types shown as gray spots.

605 **d.** Pearson correlation coefficient (red/blue colorbar) of pairwise gene expression across oocytes (rows and
606 columns) using the top 12 genes of each program identified by consensus non-negative matrix factorization (cNMF),
607 ordered by hierarchical clustering.

608 **e.** Mean expression (color) and distribution (shape, kernel density estimate) of oocyte gene programs (x axis) by the
609 enclosing follicle type (y axis). Comparison of program scores across enclosing follicle types (*$P<0.05$, **$P<0.01$,
610 ***$P<0.001$, ****$P<0.0001$, ns – not significant; two-tailed t-test).

611 **f.** Visualization of oocyte gene program usage on a principal component analysis (PCA) embedding of oocyte
612 composite transcriptomes.

613 **Extended Data Figure 2. Spatial and molecular determinants of coordination in follicular niches.**
614 **a.** Schematic depicting the radial analysis of follicles. The scaled radial distance (*r*) from the follicular center
615 (centroid, "x") of each granulosa (GC) spot was used for all radial analyses. Radially concentric bins, in increments
616 of 10 uniformly spaced bins, were used to aggregate spot-level characteristics.
617 **b,c.** Diffusion map embedding (DC2, DC3) of GCs (spots) across the luteinizing (**b**) and atretic (**c**) lineages, colored
618 by their two terminal fates ("GC – antral luteinizing", "GC – atretic"), annotated with the spot used as root (black
619 dot) for inferring the diffusion pseudotime (dpt).
620 **d.** Stability and error metrics for the selection of the optimal number of components (*k*) in cNMF analysis. Stability
621 (y axis, blue) and reconstruction error (y axis, red) were computed across *k*=3-24 (x axis) during factorization using
622 cNMF.
623 **e.** Top contributing genes to the 16 GC gene programs identified through consensus non-negative matrix
624 factorization (cNMF). Each subplot represents one of the 16 gene programs, showing the top contributing genes (x-
625 axis) and their contribution scores (y-axis). Contribution scores reflect the weight of each gene in their
626 corresponding program, highlighting genes with key roles in the biological processes captured by each program.
627 Programs 2 and 3 are annotated with functional descriptions related to FSH regulation and steroidogenesis,
628 respectively.
629 **f.** Mean expression (red colorscale; log normalized counts and variance-scaled) of GC programs (rows, columns).
630 GCs were grouped by their dominant program, defined as the program with the highest usage, then calculated for
631 their within-group mean program score.
632 **g.** Mean proportion of immune cells within follicles (y axis) by follicle type (color, lines) across the relative distance
633 from the follicle center (x axis), scaled from 0 to 1 as before; shaded lines represent the standard error of the mean
634 across follicles within each radial bin. Comparison of the immune fraction between atretic *vs* aggregated non-atretic
635 follicles containing an oocyte, based on the distribution of immune fraction across individual follicles within each
636 radial bin ($P<0.005$, Tukey HSDMann-Whitney U test; **Methods**).
637 **h.** Mean proportion of endothelial cells within follicles (y axis) by follicle type (color, lines) across the relative
638 radial distance from the follicle center (x axis), scaled from 0 to 1 as before; shaded lines represent the standard
639 error of the mean across follicles within each radial bin.
640 **i.** Circos plot of the top receptor-ligand interactions enriched in preantral (left), antral (center), and atretic (right)
641 follicles from MultiNicheNet. Interactions significantly enriched in each follicle type are shown by arrows starting
642 from ligands (bottom half) of a "sender" cell type (color) to the corresponding receptor (top half) of a
643 "receiver" cell type (color).

644 **Extended Data Figure 3. Age-associated temporal dysregulation of folliculogenesis and corpus luteum (CL)**
645 **progression.**
646 **a,b**. Distribution of follicle sizes in young (**a**) and old (**b**) mice. Boxplot of the follicle size (number of granulosa
647 spots; y axis) by follicle type (x axis) and stage (bar shading) (**P<0.005, two-tailed t-test of means). Boxplot:
648 center line indicates the median, box bounds represent the first and third quartiles, and whiskers span from each
649 quartile to the minimum or the maximum (1.5 interquartile range below 25% or above 75% quartiles).
650 **c**. Distribution of follicle pseudotime in young and old mice. Boxplot of follicle pseudotime in old and young
651 across stages. Boxplot elements: same as in **a,b**.
652 **d**. Differentially expressed genes in aging oocytes. Significance (y axis, $-\log_{10}$(P-value)) and effect size as $\log_2$fold
653 change (x axis) for genes (dots) that are differentially expressed between young and old. Significant genes (color;
654 Benjamini-Hochberg FDR<5%, log2FC>1) are annotated with select genes.
655 **e.** Mean expression in oocytes (log normalized counts and variance-scaled) of *Nlrp9*-family genes (columns)
656 grouped by the enclosing follicle type (rows), in young (left) and old (right) mice.
657 **f.** Distribution of immune spot proportion in CL segments. Boxplot of percentage of immune spots calculated per
658 segment (y axis) by stage (x axis) and CL segment ytpe (bar shading) (**P<0.005, ***P<0.0005; two-tailed t-test
659 of means). Boxplot elements: same as in **a,b**.

660 **Extended Data Figure 4. Global changes in aged ovaries.**

661 **a.** Distribution of cell type composition (y axis) across pucks (dot) and the mean composition across pucks (bars)
662 within each age group (color). Credible and significant changes determined by scCODA indicated by black bars
663 (**Methods**).

664 **b.** Differentially expressed genes in aging stromal cells (fibroblasts, stromal – nonsteroidogenic, stromal –
665 steroidogenic). Significance (y axis, $-\log_{10}$(P-value)) and effect size as $\log_2$-fold change (x axis) for genes (dots)
666 that are differentially expressed between young and old. Significant genes (color; Benjamini-Hochberg FDR<5%,
667 log2FC>1) are annotated with select genes.

668 **c.** Pearson correlation coefficient (colorbar) of pairwise gene expression across immune spots (rows and columns)
669 using the top genes of each program identified by consensus non-negative matrix factorization (cNMF), ordered by
670 hierarchical clustering.

671 **d.** Mean expression of immune program 3 (y axis) associated with pro-inflammatory signatures across the relative
672 distance from the follicle center (x axis), scaled from 0 to 1. Shaded line: standard error of the mean across follicles
673 within each radial bin. Expression bins are separated by follicle type (color) among young mice (left) and old mice
674 (right).

675 **e.** Transcriptional signatures of multi-nucleated giant cells (MNGCs). Stromal immune spots were separated into
676 four categories based on age (young *vs* old) and MNGC content (low *vs* high), then examined for differentially
677 expressed genes across these four categories. Mean expression (log normalized counts, dot color) and proportion of
678 expressing stromal immune cells (dot size) of differentially expressed genes (columns) in each age-MNGC category
679 (rows).

680 **Extended Data Figure 5. Identifying contaminated oocyte spots using non-negative matrix factorization**
681 **(NMF).**
682 Two iterations of oocyte spot decontamination.
683 **a-d.** Identifying contaminated oocyte spots through a two-step iteration, with the first iteration in **a,b** to remove
684 contaminant spots, followed by a second iteration in **c,d** to further remove residual contaminants.
685 **a,c.** Gene programs identified through NMF on oocyte spots using *k*=8 programs. Correlation scores (left, x axis)
686 of the top 12 genes (left, y axis) and their program usage on a UMAP projection (right) of oocyte spots. Programs
687 identified as contamination based on the expression of known cumulus and granulosa marker genes are labeled as
688 'Contaminant' (first iteration: programs 1, 2, 4, and 6; second iteration: program 1).
689 **b,d.** Distribution of program scores (y axis, kernel density estimate) grouped by the top gene program (x axis) for
690 each spot (dots). Distributions were used to manually set program-specific thresholds for removing contaminants.
691 First iteration thresholds: Program 1: > 0.4, Program 2: > 0.3, Program 4: > 0.3, Program 6: > 0.4. Second iteration
692 thresholds: Program 1: > 0.3.

693 **METHODS**

694 **Mice.**

695 *Buck mice.* Female C57BL/6J (Jax 000664) mice were bred at the University of San Francisco (UCSF). All mice
696 were maintained under SPF conditions on a 12-hour light-dark cycle, at ambient temperature 21.5 + 1˚C and relative
697 humidity between 30% and 70% and provided food and water ad libitum. All mouse experiments were approved
698 by and performed in accordance with the Institutional Animal Care and Use Committee guidelines at UCSF on a
699 mouse protocol under Zachary Knight.

700

701 *Broad mice*. Female C57BL/6J (Jax 000664) mice were purchased from The Jackson Laboratory at ages 10, 36,
702 and 50 weeks. Mice were acclimated to the vivarium for 2 days ("Broad cohort 1") or 2 weeks ("Broad cohort 2")
703 upon arrival. All mice were maintained under SPF conditions on a 12-hour light-dark cycle, at ambient temperature
704 21.5 $\pm$ 1˚C and relative humidity between 30% and 70% and provided food and water ad libitum. All mouse
705 experiments were approved by and performed in accordance with the Institutional Animal Care and Use Committee
706 guidelines at the Broad Institute on a mouse protocol under H.C. and F.C.

707

708 **Estrous cycle staging mice by vaginal cytology.**

709 *Buck mice.* Mice collected at UCSF were staged near-daily for 8 consecutive days using vaginal cytology, as
710 previously described[110,111]. A total volume of 100 µL sterile saline (in 20-50 µL increments) was expelled 5-10
711 times with a P200 pipette into the vaginal canal, taking care to avoid touching the vaginal opening with the pipette
712 tip then expelled onto a glass slide and imaged immediately using Nikon Eclipse Ts2 (10X objective) and a Nikon
713 DS Qi2 camera.

714

715 *Broad mice.* Female mice were staged near-daily for 8 consecutive days using vaginal cytology, as previously
716 described[110,111]. Briefly, mini-tip flocked nasopharyngeal swabs (VWR SLIN501CS01) were moistened with sterile
717 PBS, and ~1/4th of the flocked tip was inserted into the vaginal canal of manually restrained mice. Swabs were
718 rotated 5 times clockwise, 5 times counterclockwise, and then smeared onto a non-treated glass slide (VWR #16004-
719 422). Slides were air-dried and stained with a 0.1% crystal violet solution (Jorgenson #J0322) for 1–2 minutes.
720 Excess stain was rinsed with PBS and sterile water, and the slides were counterstained with 1% eosin (Jorgenson
721 #J0322A) for 10–20 seconds. Following the counterstaining step, slides were rinsed again, air-dried completely,
722 examined under a light microscope, and imaged with a Leica Aperio VERSA Brightfield, Fluorescence & FISH
723 Digital Pathology Scanner, using the 20x objective.

724

725 Cytology evaluation identified the predominant cell types (epithelial cells, cornified cells, and leukocytes), enabling
726 the classification of the estrous cycle stages (proestrus, estrus, metestrus, and diestrus) as previously described[110,111].
727 In brief, proestrus, estrus, and diestrus are characterized by a predominance of nucleated epithelial cells, cornified

728 epithelial cells, or leukocytes, respectively, while metestrus is identified by a mixture of cornified epithelial cells
729 and leukocytes[112,113]. The time course of the estrous cycle is in **Extended Data Table 1**.
730
731 **Tissue collection.**
732 Once identified to be in the appropriate estrous stage for collection, mice were placed under anesthesia with 3%
733 isoflurane for 1 minute and maintained via a nose cone flowing 1% isoflurane. Anesthesia was confirmed by the
734 absence of a pedal reflex. Transcardial perfusion was performed with PBS through the left ventricle to remove blood
735 from tissues before entire ovaries were removed and immediately frozen on dry ice in a cryomold containing
736 Optimal Cutting Temperature (OCT) compound. Tissues were then either processed immediately or stored at -80°C
737 for storage.
738
739 ***In situ* transcriptome processing via Slide-seq.**
740 Tissue sections were processed and sequenced using Slide-seq v2 as previously described[5]. Slide-seq arrays were
741 purchased from Curio Biosciences (Curio Seeker) or prepared in-house using custom-synthesized barcoded beads
742 functionalized with the sequence[28]
743 (5'TTT_PC_GCCGGTAATACGACTCACTATAGGGCTACACGACGCTCTTCCGATCTJJJJJJJJTCTTCAGC
744 GTTCCCGAGAJJJJJJNNNNNNNNVVT30-3') with a photocleavable linker (PC), a bead barcode sequence (J, 14
745 bp), a UMI sequence (NNNNNNNNVV, 9 bp), and a poly dT tail. The sample table of all Slide-seq data, denoting
746 the puck origin and other metadata, is in **Extended Data Table 2**.
747
748 OCT-embedded frozen tissue samples were warmed to -20°C, sectioned to 10 µm on a cryostat (Leica CM3050S),
749 placed on a pre-cooled Slide-seq array and melted onto the array by warming it briefly. For each sample, 2-3 sections
750 for Slide-seq were collected >200 µm to maximize sampling diversity of tissue sub-structures and consecutive
751 sections were collected for hematoxylin and eosin staining. The affixed tissue section and array was moved into a
752 1.5 mL Eppendorf tube for tissue digestion and transcriptomic library preparation as previously described[5,6]. The
753 last library amplification was performed in a final volume of 200 µL of PCR mix, divided into four 0.2 ml tubes
754 and cycled with the following program: 1 cycle of 98°C for 2 min, 4 cycles of 98°C for 20 s, 65°C for 45 s, 72°C
755 for 3 min, 9 cycles of 98°C for 20 s, 67°C for 20 s, 72°C for 3 min, and 1 cycle of 72°C for 5 min. Libraries were
756 sequenced using the following read structure on a NextSeq 1000/2000 (P2; Illumina) or NovaSeq (S4 or X;
757 Illumina): Read1: 42 bp; Read2: 50bp; Index1: 8 bp, and sequences were processed as previously described[5] using
758 the pipeline available at (https://github.com/MacoskoLab/slideseq-tools).
759
760 **Hematoxylin and eosin stain of adjacent histology sections.**
761 Serial sections of 10 µm thickness were obtained from the frozen tissue samples and mounted onto glass microscope
762 slides (VWR SuperForst 48311-703). Using a Leica ST5010 Autostainer XL (Leica Biosystems), sections were
763 immersed in xylene, sequentially processed through a graded ethanol series (100% and 95%), and then stained with

764 hematoxylin (Leica Biosystems 3801571). The nuclei were differentiated with mild acid treatment (Leica
765 Biosystems 3803598), followed by "bluing" through exposure to a weakly alkaline solution (Leica Biosystems
766 3802918) and subsequent water washing. Sections were then stained with Eosin (Leica Biosystems 3801616),
767 processed through a graded ethanol series (100% and 95%), xylene, dehydrated, and finally coverslipped using the
768 Leica CV5030 Fully Automated Glass Coverslipper. Brightfield images were captured with the Leica Aperio
769 VERSA Brightfield, Fluorescence & FISH Digital Pathology Scanner, using the 20x objective.
770
771 **Pre-processing of spatial transcriptomics data.**
772 Raw sequencing reads were demultiplexed using Cellranger (v.6.1.2) mkfastq (10x Genomics)[114] and aligned to
773 the mouse mm10 reference genome using STAR v2.7.8a with default parameters[115]. Spatial barcode assignment
774 and bead-based feature extraction were performed using the Slide-seq pipeline (v2022-01-01) and represented as
775 a gene-by-spot expression matrix directly within the Slide-seq pipeline for downstream analyses[5,6].
776
777 **Initial data processing.**
778 Gene expression data of individual pucks were concatenated using an outer join. Spatial coordinates were assigned
779 by matching barcodes from puck-specific barcode matching files. Metadata, including puck and sample IDs, estrous
780 stage, and animal age category, were appended to the AnnData object. The combined dataset was filtered to retain
781 spots with at least 50 detected genes and 150 UMI counts. For spot clustering and embeddings, all gene expression
782 values were scaled and centered. The top 5,000 highly variable genes were identified from log-normalized counts
783 across all batches using Scanpy's highly_variable_genes function (batch key=puck)[116]. Dimensionality reduction
784 was conducted by first regressing out total UMI counts on log-normalized counts, then conducting principal
785 component analysis (PCA) on highly variable genes, followed by correcting for puck-specific batch effects using a
786 PyTorch implementation of Harmony[117], then constructing a nearest-neighbor graph with k=10 neighbors using the
787 top 40 principal components. Unsupervised clusters of spots were identified with the Leiden algorithm[94]
788 (resolution=1.5) and visualized using UMAP[118], all implemented in Scanpy[116] (v1.10.1).
789
790 *Smear removal.*
791 Smearing artifacts were manually identified and removed using an interactive selection tool. Spatial scatter plots
792 were generated using Squidpy to visualize cell spots color-coded by cluster identity[97]. Using an interactive
793 LassoSelector widget, regions of spots suspected of containing technical artifacts were removed and excluded from
794 further analyses. This process was repeated for each puck, resulting in refined AnnData objects free from smear
795 artifacts. Following smear removal, the dataset was re-processed to refine dimensionality reduction and clustering
796 as described above, resulting in a total of n=601,831 spots from 68 spatial transcriptomes.
797
798 **Unsupervised clustering and cell type annotation.**

Cell types were annotated using top differentially expressed genes (DEG) identified for each Leiden cluster and cross-referenced with established marker genes from literature[35,38,66,103,109,119–123]. DEGs were identified using Scanpy's rank_genes_groups function with the Wilcoxon rank-sum test to detect cluster-specific marker genes. Spatial scatter plots and UMAP embeddings were used to visualize marker gene expression and confirm cluster-specific identities. Granulosa cells (GCs) were further subclustered by re-running Leiden clustering on GC subsets, followed by DEG analysis and marker-based assignment. The top 50 marker genes identified for each cluster are in **Extended Data Table 3.**

Spatial segmentation of oocytes, follicles, and corpora lutea (CL).

Code underlying these analyses can be found in II.2_segmentation.ipynb and II.3_segment_extension.ipynb.

Oocyte segmentation.

We defined spots in the 'Oocyte' or the 'Oocyte - cumulus' spot cluster as putative oocyte spots. 'Oocyte - cumulus' spots were included in initial segmentation to ensure robustness against variations in cluster boundaries between 'Oocyte' and 'Oocyte - cumulus' spots but were subsequently removed from the final oocyte segments as described below. For each puck, a spatial neighborhood graph of putative oocyte spots (radius=50) was constructed and clustered with the Leiden algorithm[124] (resolution=0.1) to define preliminary oocyte segments. 'Oocyte - cumulus' spots were then removed from these segments. Segments containing fewer than three spots were also discarded. Final oocyte segments were further refined through subclustering, merging, and manual curation based on tissue context. Details of these curation choices are documented in the supplementary code.

Additional decontamination of cumulus spots from oocyte spots.

Non-negative matrix factorization (NMF)[125] was used to identify gene programs corresponding to cumulus cell contamination in spots labeled as oocyte from Leiden clustering. scikit-learn[126] was used to perform NMF with k=8 programs on log1p normalized counts. Programs 1 (*Kctd14*, *Slc18a2*, *Wt1*), 2 (*Lars2*, *Hexb*, *Cdk8*), 4 (*Inhba*, *Inhbb*, *Nap1l5*), and 6 (*Col1a2*, *Col3a1*, *Cfh*) were identified as contaminating signals based on their constituent genes (**Extended Data Fig. 5a**). Spots were annotated as contaminants if they either had these programs as their top utilized program or if the program scores reached the following thresholds: Program 1: > 0.4, Program 2: > 0.3, Program 4: > 0.3, Program 6: > 0.4 (**Extended Data Fig. 5b**). Spots annotated as contaminants were removed from the object before a second round of decontamination was performed on remaining spots using NMF with k=8 programs. Program 1 (*Serpine2, Ccnd2, Kctd14*) was identified as a contaminating signal based on its constituent genes (**Extended Data Fig. 5c**). Spots that had this program as the top utilized program, or had a program score >0.3 were annotated as contaminants (**Extended Data Fig. 5d**) and removed from the oocyte segments for the computation of these averages.

Identifying primordial oocytes.

835 To identify any remaining small, putatively primordial, oocytes, unassigned spots labeled as 'Oocyte' or expressing
836 primordial oocyte marker gene *Sohlh1*[34,56] that were at least 200 from an oocyte segment center were selected. A
837 spatial neighborhood graph of these putative primordial oocyte spots for pucks containing at least two such spots
838 using a radius of 20 µm to account for the expected small size of these primordial oocytes. Oocyte segments were
839 identified after Leiden[124] clustering (resolution=0.1). Spots labelled as 'Oocyte - cumulus' were removed from these
840 segments. Segments containing less than 2 spots or lacking *Sohlh1* expression were excluded.
841
842 *Segmentation of follicles and corpora lutea (CL).*
843 Spots in the 'Cumulus – oocyte', 'GC – preantral', 'GC - antral early mitotic', 'GC - antral luteinizing', 'GC - antral
844 mitotic', 'GC – atretic' clusters were defined as putative follicle spots, while spots in the 'Luteal - early', 'Luteal -
845 late' clusters were defined as putative CL spots. A spatial neighborhood graph of the putative follicle and CL spots
846 (radius 50 µm) was constructed and clustered with Leiden[124] (resolution=0.1 for follicles and a smaller
847 resolution=0.001 for CLs because they tended to be larger) for each puck, yielding segments. Segments with less
848 than 20 spots were removed, the remaining were then subclustered and merged as appropriate based on manual
849 inspection. These curation choices are documented in the supplementary code. Segments were then extended to
850 include additional spots from the selected GC or luteal cell types, respectively, within 50 µm of a spot already
851 assigned to a segment or the next closest segment if multiple were within 50 µm.
852
853 In a few cases, oocyte segments had been identified by the above oocyte segmentationbut the corresponding follicle
854 was either too small or irregular, resulting in partial or complete omission by this follicle segmentation pipeline. To
855 address these cases, unassigned spots from the above selection of follicle cell types within 50 µm of an oocyte
856 segment were assigned as follicle segments and grouped based on the closest oocyte segment. If these new follicle
857 segments were closer than 100 µm (minimal spotspot distance across a segment pair) to existing follicle segments,
858 the segments were merged.
859
860 To capture remaining small follicles, unassigned spots in the 'Cumulus – oocyte', 'GC – preantral', 'GC - antral
861 early mitotic', and 'GC – atretic' spot clusters were defined as mapping to putative small follicles. Within each
862 puck, one spatial neighborhood graph was each constructed for these putative follicle and CL spots (radius 20 µm)
863 and clustered with Leiden (resolution=0.1), resulting in additional segments. Segments with less than 5 spots
864 assigned were removed. Remaining segments were merged with existing follicle segments if they were within 50
865 µm of existing segments (minimal spot-spot distance across segment pair). The final segments were further
866 subclustered, merged, and reassigned to proximal oocytes as appropriate. These curation choices are documented
867 in the supplementary code.
868
869 *Assigning proximal spots to segments.*

870 Immune ('Immune'), endothelial (all 'Endothelial' types), theca ('Theca' and 'Stromal - steroidogenic'), and
871 mesenchyme ('Adipocyte', 'Stromal - nonsteroidogenic') spots were assigned to follicle or CL segments that were
872 less than 100 µm away.
873
874 *Assigning oocytes to follicles.*
875 Oocyte segments were assigned to the closest follicle segment if it was less than 100 µm away. These assignments
876 were manually curated where appropriate based on manual inspection of the segmentation results and the
877 surrounding tissue; these curation choices are documented in the supplementary code.
878
879 **Follicles and corpora lutea (CL) segments labeling.**
880 First, segments were assigned as follicle or CL: CL segments were classified as those in which the most frequent
881 spot type was a luteal type, or where the sum of the fraction of luteal types out of above granulosa (GC) and luteal
882 types was larger than 50%; all remaining segments were classified as follicles. (**Extended Data Fig. 1a, b**). Note
883 that this classification was performed on all segments from both the follicle and CL segmentation above to recover
884 exceptional cases in this initial segmentation. Second, more specific state labels were assigned to the resulting
885 follicle and CL segments. Follicle segments were labelled as 'Follicle – atretic' if more than 20% of their assigned
886 spots were classified as 'GC – atretic'. All other follicle segments were classified based on their most abundant GC
887 type ('GC – preantral' as 'Follicle – preantral', 'GC – antral luteinizing' as 'Follicle – antral luteinizing', 'GC –
888 antral early mitotic' and 'GC – antral mitotic' as 'Follicle – antral mitotic'). CL segments were classified as 'CL -
889 early' and 'CL – late' based on their majority luteal cell type.
890
891 **Calculating mean expression profiles of oocyte, follicle and corpus luteum (CL) segments.**
892 Raw (unfiltered and un-normalized) counts of spots assigned to a segment (either oocyte, follicle, or CL were
893 normalized per spot to 10,000, then averaged within each segment. Where appropriate, the resulting segment
894 expression profiles were log1p transformed for downstream analyses.
895
896 **Identifying gene programs with non-negative factorization.**
897 *Oocytes.*
898 Gene programs in composite oocytes were identified using scikit-learn[126] to perform non-negative matrix
899 factorization (NMF)[125]. Log-normalized counts were used for NMF (k=5 programs) to reduce the noise of highly
900 expressed genes in composite oocytes that were composed of few oocyte spots. To interpret the biological relevance
901 of the gene programs, genes were ranked for each program by their contributions to the gene weight matrix. Program
902 usage across oocytes were visualized using PCA embeddings.
903
904 *Granulosa cells (GCs).*

905 Gene programs in GCs were identified using consensus non-negative matrix factorization (cNMF), following the
906 workflow described by Kotliar et al[65]. Using raw gene expression counts as input, 5,000 highly variable genes
907 (HVGs) were identified by calculating gene variance across spots during preprocessing with the top 5,000 HVGs
908 retained for downstream analyses. Batch correction was incorporated directly into the cNMF pipeline using an
909 adapted version of Harmony[117] and the resulting corrected matrix, with negative values set to zero, resulting in the
910 batch-corrected matrix used for factorization. cNMF was run on the corrected matrix to factorize the expression
911 data into two components: a gene weight matrix, in which each gene is associated with specific programs, and a
912 usage matrix, in which each spot is assigned a score reflecting its degree of program activity. The number of
913 programs (k) was set to 16, determined by running cNMF over a range of program numbers (k = 3 to 24) and
914 selecting the *k* with maximal program stability, calculated as the Pearson correlation between factorization results
915 across 20 replicates for each *k* (**Extended data Fig. 2d**). For the selected *k*, cNMF was re-run with 200 replicates
916 to generate final consensus matrices and extract robust and biologically meaningful programs.
917
918 To interpret the biological relevance of the gene programs, genes were ranked for each program by their
919 contributions to the gene weight matrix (**Extended data Fig. 2e**). Program activity scores were normalized per spot
920 by dividing the raw usage matrix values by the total program activity per spot. Spots were grouped by their dominant
921 GC program, defined as the program with the highest normalized usage score, to assess program separation and
922 overlap (**Extended data Fig. 2f**). Gene programs were annotated by comparing the top contributing genes against
923 known GC markers and enriched functional pathways from the literature[14,17,23,127,128].
924
925 *Immune.*
926 To identify gene programs in immune cells, the same workflow for consensus non-matrix factorization (cNMF) as
927 described for GCs was followed. Long non-coding RNAs genes with the prefix 'Gm' were filtered out to remove
928 noise, removing 6933 genes, resulting in an input matrix of 41879 immune cells x 20370 genes. After filtering the
929 raw gene expression counts were used as input for cNMF. Highly variable genes (HVGs) were identified the same
930 way as with GCs, through the calculation of gene variance. For further downstream analysis the top 5000 HVGs
931 were retained. After running cNMF, the number of programs (k) was set to 14, as it balanced stability and error
932 from the range of k values from 5-25. Overall error decreases as the number of programs increases but stability was
933 found to be variable throughout program values, resulting in a need to balance the two metrics.
934
935 Similar to the analysis conducted with the GCs, genes with the highest contribution to the gene weight matrix were
936 investigated. Programs with top genes not known as canonical immune markers were not used for downstream
937 analysis, and were assumed as noise, resulting in the first 6 programs being established as immune programs.
938
939 **Compositional analysis of cell and segment types.**
940 *Cell-type composition within segments analysis.*

941 For each relevant predicted cell type, the fractional composition was computed as the proportion of spots assigned
942 to that cell type within each segment. The mean and standard error of these fractions were calculated across
943 segments and grouped by distinct segment types. These results were used to analyze patterns in cell type
944 composition and visualize the relative contributions of different cell types and segments.
945
946 *Segment type composition analysis.*
947 The relative abundances of different segment types, including follicular and corpus luteum segments, was
948 analyzed across estrous stage and animal age. The proportions of each segment type (e.g., preantral, antral mitotic,
949 antral luteinizing, and atretic segments) were calculated as the fraction of individual segments of the same
950 segment type within each sample (puck). Mean fractions and standard errors were computed across pucks for each
951 experimental condition, grouped by estrous stage and animal age. Statistical differences between the fraction of a
952 particular segment type across different groups of pucks were assessed with t-tests, and significant differences
953 were highlighted in visualizations.
954
955 **Trajectory inference of granulosa cells (GCs).**
956 Trajectory inference of GCs was performed using diffusion pseudotime (dpt), a graph-based method that models
957 cellular transitions along a continuum, as described in previous single-cell RNA-seq studies[63]. Dpt analysis was
958 conducted on annotated GCs after dimensionality reduction using principal component analysis (PCA). A k-nearest
959 neighbor (k-NN) graph was constructed using the top 40 principal components, with k set to 10, to define local
960 cellular neighborhoods. Diffusion components (DCs) were computed from the neighborhood graph to capture the
961 structure of cellular transitions in high-dimensional space. The root of the trajectory was manually selected based
962 on inspection of DC embedding. Dpt values were calculated separately for two GC subsets: (1) all spots within
963 antral mitotic and antral luteinizing follicles, and (2) all spots within atretic follicles. This allowed for separate
964 modeling of GC trajectories under different follicular conditions. The inferred trajectories captured the progression
965 of GC states from early mitotic stages to luteinization and atresia, consistent with known GC maturation pathways.
966
967 **Calculation of cell cycle scores.**
968 To assess cell cycle dynamics in annotated granulosa cell spots in young mice, canonical markers of S-phase and
969 G2/M-phase, as previously described[129], were used to calculate cell cycle phase scores. Based on these scores, spots
970 were classified into three phases: G1, S, or G2/M. Spots classified as G1 were further categorized as "Non-Cycling,"
971 while spots in S or G2/M phases were categorized as "Cycling." This classification was integrated with spatial
972 transcriptomic data to map the cycling status of annotated granulosa spots. Dimensionality reduction methods were
973 applied to visualize cell cycle phases in relation to spatial organization in tissues, enabling an analysis of
974 proliferative activity within granulosa cell-associated regions of the ovary.
975
976 **Radial distance analysis within segments.**

977 To examine spatial trends in our analysis, radial distances for spots within follicular segments were computed. The
978 radial distance for each spot was calculated as the Euclidean distance from the centroid of the segment, scaled by
979 the maximum segment radius. This normalized distance, referred to as the "scaled radial distance," enabled a
980 standardized comparison of spatial patterns across segments of varying sizes. Spots were binned along the scaled
981 radial distance into equal intervals of 10 spanning the range [0, 1] (**Extended Data Fig. 2a**).
982
983 For each radial bin, the mean and standard error of the mean (SEM) of various features such as cell type
984 composition, dpt and cell cycle scores, cNMF-derived gene program usage were first calculated across individual
985 bins. Each mean and SEM were then aggregated for each distance bin within the same segment type. Segment-
986 specific trends were then visualized by plotting the mean proportions or cNMF program scores for each distance
987 bin, with shaded regions representing the SEMs.
988
989 To evaluate spatial trends in various features across scaled radial distance bins, the monotonic relationship between
990 the radial bin index (independent variable) and the mean values of the feature of interest (e.g., cell type composition,
991 cell cycle state, dpt, or cNMF program usage) for each segment type was assessed using Spearman rank correlation.
992 For each segment type, the mean feature values within each radial distance bin were calculated as described above
993 and correlated with the corresponding radial distance bins to determine whether the feature of interest varied
994 systematically with distance from the segment centroid. Spearman correlation was chosen for its robustness in
995 detecting monotonic relationships, regardless of the underlying distribution or linearity. The Spearman correlation
996 coefficient (ρ) and associated p-value were calculated using the SciPy library. Bins with fewer than two data points
997 were excluded from the analysis.
998
999 **Follicle embedding and trajectory inference using optimal transport.**
1000 Code underlying these analyses can be found in III_segment_OT_1_pca_coretypes.ipynb and
1001 III_segment_OT_2_plot_results.ipynb.
1002
1003 *Segment-to-segment distance matrix computation.*
1004 A distance matrix was computed between any pair of segments of all follicle and corpus luteum (CL) segments in
1005 young mice. For each segment, oocyte, granulosa or luteal spots, and theca spots were considered. A transport
1006 matrix from spots in any pair of segments was calculated with optimal transport, using the Sinkhorn algorithm
1007 implemented in moscot[67] (epsilon=0, tau_a=1., tau_b=1., rank=20, initializer=k-means, min_iterations=5,
1008 max_iterations=200). This transport matrix was multiplied elementwise with the cost matrix of the optimal transport
1009 problem and the sum over all elements in this resulting matrix was used as a distance measure between the two
1010 segments.
1011
1012 *Segment embedding and follicle pseudotime.*

1013 This segment-to-segment distance matrix was treated as a segment feature space. The k-nearest neighbor graph of
1014 segments (k=15) was built from the top 50 PCAs computed and embedded as a UMAP. This embedding was
1015 generated both for the union of all follicle and CL segments in young mice, and for follicles in young mice alone.
1016 Diffusion pseudotime[112] was then computed for follicles in young mice based on a manually defined root segment.
1017
1018 *Trajectory projection of follicles from middle-aged and old mice.*
1019 A distance matrix was calculated between all follicle and CL segments in young mice and middle and old mice,
1020 using the same optimal transport approach as above. Each segment from middle and old mice was then assigned to
1021 its closest neighbor in young mice based on this distance. Follicles from middle and old mice were then assigned
1022 the pseudotime coordinates from their closest neighbor follicle in young mice.
1023
1024 **Cell–cell communication analysis.**
1025 Code underlying these analyses can be found in
1026 III.5_nichenet_ageYoung_stageAll_segmentFollicle_withOocyte_byCluster.Rmd and
1027 III_segment_OT_2_plot_results_v0.3.ipynb.
1028
1029 Cell-cell communication analysis was performed with MultiNicheNet[68] on data from young mice, with follicle
1030 segments considered as samples for the purpose of the algorithm. Comparisons were performed between different
1031 follicle labels, using coarse cell type labels (preantral, antral, atretic). Oocyte, granulosa, theca, and immune spots
1032 were included in this analysis. Ligand-receptor pairs and receiver-sender cell type pairs specific to each follicle
1033 label were prioritized accordingly. Follicles that did not meet default cell type compositional thresholds were
1034 discarded (at least 5% of spots per segment mapping to each cell type). To characterize the communication states
1035 across all follicles, a summarized ligand-receptor score was calculated for each segment. This score was derived
1036 first by calculating the mean of normalized expression of receptor and ligand pairs for all cell types within a
1037 segment, log1p transforming, and then summed to generate the final segment specific ligand and receptor score.
1038
1039 **Immune infiltration analysis.**
1040 To compare the infiltration of immune cells across segment types, immune spot composition was analyzed relative
1041 to distance from the segment center. For each scaled radial distance bin (calculated as described above) within
1042 individual segments, the proportion of immune spots was calculated by dividing the number of immune spots by
1043 the total number of spots within each bin. The average immune composition and standard error of the mean (SEM)
1044 for each distance bin were determined for every segment type to assess systematic variation with distance from the
1045 segment center. Tukey's Honest Significant Difference (HSD) test was applied to evaluate the monotonic
1046 relationship between the radial bin index (independent variable) and the mean values of the feature of interest
1047 (dependent variable) for each segment type. To address potential bias from tissue sectioning, additional analysis
1048 was conducted on oocyte-containing follicles to confirm that slicing artifacts did not affect the evaluation of radial

1049 infiltration (**Extended Data Fig. 2g**). Statistical comparisons and p-values were calculated using the SciPy library.
1050 Radial bins with fewer than two data points were excluded from both statistical and visualization analyses.
1051
1052 **Age-associated differential gene expression analysis.**
1053 *Follicles.*
1054 To analyze key hormone gene changes across young and old follicles, mean gene expression was calculated as
1055 described above. For each segment type (preantral, antral mitotic, antral luteinizing, and atretic follicles), stage
1056 (Estrus, Metestrus) and age, mean and SEM of gene expression were calculated for the hormone-related genes
1057 *Amhr2*, *Fshr*, *and Lhcgr*[43]. Differential expression analysis between estrous stages was performed using two-sided
1058 t-test.
1059
1060 *Oocytes.*
1061 Primordial oocytes were removed from analysis due to the low representation in old animals. Genes were filtered
1062 to remove those expressed in less than 10% of oocytes. Differential expression analysis was performed using Scanpy
1063 on young and old oocytes, using log1p normalized data using t-test with overestimated variance and using the
1064 Benjamini-Hochberg correction method. Genes with a p-value <0.05 and a log2 fold change >1 were used for further
1065 analysis.
1066
1067 *Stromal cells.*
1068 Stromal cells including spots labeled as fibroblasts, stromal – nonsteroidogenic, and stromal – steroidogenic were
1069 used for differential expression analysis. Genes were filtered to remove those expressed in less than 10% of spots.
1070 Differential expression analysis was performed using Scanpy on young and old spots, using raw counts using t-test
1071 with overestimated variance and using the Benjamini-Hochberg correction method. Genes with a p-value <0.05 and
1072 a log2 fold change >1 were used for further analysis.
1073
1074 **Cell-type compositional analysis.**
1075 The spot composition for each cell type was calculated for each puck. Mean composition was then calculated for
1076 young, middle, and old ages for each cell type. To determine significance of cell composition changes with age, the
1077 scCODA package was used[90], with young used as the control group, and epithelial – oviduct as the reference cell
1078 type, as its composition has low variation across conditions. Subsets of immune spots were created based on their
1079 segment assignments to follicles or corpora lutea (CL), or stroma if unassigned. Endothelial spots localized to CL
1080 were subset from other endothelial spots.
1081
1082 **Identifying multi-nucleated giant cells (MNGCs).**
1083 Code underlying these analyses can be found in II.5_registration_v0.8_all_pucks.ipynb and
1084 III_MNGC_dotplot_v0.1.ipynb.

1085

1086 *Annotation of MNGCs in histology sections.*

1087 Manual annotation of histology sections adjacent to sections used for Slide-seq analysis were used to classify the
1088 presence of multi-nucleated giant cells (MNGCs) based on pigmentation, size, and proximity to a growing follicle
1089 as previously described[11,31,91,98,99]. H&E stains with a high density of light brown clusters, generally surrounding
1090 growing follicles, were categorized as "visible MNGCs" (19 samples). Sections with lighter pigmentation and a
1091 lower density of clusters were categorized as "possible MNGCs" (13 samples). Samples lacking visible
1092 pigmentation were labeled as "no MNGCs."

1093

1094 *Segmentation of MNGCs in H&E and registration with spatial transcriptomics data.*

1095 Samples deemed to contain MNGCs upon visual inspection of the H&E images were selected for segmentation.
1096 H&E images and spot transcriptomics were registered using a napari plugin in squidpy[130], with anchor points
1097 manually defined at tissue features clearly visible in both (such as large oocytes or points on the edges of the tissue
1098 section). In this registered space, spots within MNGC regions were segmented based on histology and spot
1099 transcriptomics. For the analysis of immune cells in stroma and MNGC, all immune spots outside of follicle or
1100 corpus luteum segments were selected and classified as "stromal" (outside of MNGC segments) and "MNGC"
1101 (inside of MNGC segments).

1102

1103 **Co-localization analysis of segmented tissue structures.**

1104 Code underlying these analyses can be found in III_segment_colocalization.ipynb. Within each puck, a spatial
1105 neighborhood graph of follicles was constructed to represent each follicle by the spatial center point of its constituent
1106 spots. Neighborhood enrichment was performed on this graph with Squidpy[130] within homotypic follicles (preantral,
1107 antral, and atretic) with varying radius from 200 μm to 2000 μm in steps of 200 μm.

1108

1109 **Lead contact.** Further information and requests for resources and reagents should be directed to and will be fulfilled
1110 by the lead contact, Hattie Chung (hattie.chung@yale.edu)

1111

1112 **Data availability.** All sequencing data (Slide-seq) and expression count matrices (Slide-seq) will be deposited in
1113 Gene Expression Omnibus and the cellxgene portal prior to publication.

1114

1115 **Code availability.** All code is available at https://github.com/HattieChungLab/ovarian_aging

1116

1117 **Author contributions**

1118 H.C. and J.G. designed the study. H.C., A.K., I.B., and S.M. conducted the pilot experiment and analysis. A.K.,
1119 H.C., and T.C.T.L. conducted the mouse work. G.M. created in-house Slide-seq tiles with supervision from F.C.
1120 R.R., T.C.T.L., and H.C. conducted Slide-seq experiments. R.R. and T.C.T.L conducted histology experiments and

imaging. R.R. processed all Slide-seq data. T.C.T.L. and A.K. conducted cell type clustering analyses and annotation under supervision by H.C., D.S.F., A.K.S., and P.C.S. D.S.F. designed and implemented the segmentation pipeline, optimal transport, and cell-cell interaction analyses. D.S.F., R.R., and R.S. conducted computational histology analyses. H.C. and D.S.F. designed and supervised all other analyses conducted by T.C.T.L., A.K., S.S., A.M., and H.T. H.C. and J.G. supervised the overall project. T.C.T.L., D.S.F., A.K., R.R., S.S., and H.C. interpreted the results with input from all authors. H.C., D.S.F., A.K., J.G., and T.C.T.L. wrote the paper with input from all authors. All co-first authors contributed equally.

Acknowledgments

This work was funded by a Pilot Grant from the Productive Health Global Consortium (formerly GCRLE) awarded to H.C. H.C. also acknowledges support from start-up funds from Yale University. T.C.T.L. is in part supported by the Productive Health Pilot Grant awarded to H.C. D.S.F. is supported by the Eric and Wendy Schmidt Center fellowship at the Broad Institute. J.L.G. and A.K. are supported by the NIH (R35 GM145305). We thank the Broad Institute vivarium staff, especially Nathan Chan, for assistance with vaginal cytology. We thank Nicholas S. Moore for helpful feedback on the manuscript, and all members of the Chung and Garrison Labs and Francesca E. Duncan for helpful discussions.

Competing interest declaration

A.K.S. reports compensation for consulting and/or scientific advisory board (SAB) membership from Honeycomb Biotechnologies, Cellarity, Danaher, Ochre Bio, Bio-Rad Laboratories, Relation Therapeutics, IntrECate biotherapeutics, Parabalis Medicines, Passkey Therapeutics and Dahlia Biosciences unrelated to this work. P.C.S. is a co-founder of Sherlock Biosciences and Delve Biosciences, a board member of Polaris Genomics, a former board member of Danaher Corporation, and a former scientific advisory board member of NextJenGane, and holds equity in the companies unrelated to this work. F.C. is a founder of Curio Bioscience and Doppler Bio. All other authors report no potential conflicts.

Supplemental Information

Extended Data Figures 1-5

Extended Data Tables 1-3

1150 **References**

1151 1. Bieuville, M. *et al.* Number of lifetime menses increases breast cancer occurrence in postmenopausal
1152 women at high familial risk. *Front. Ecol. Evol.* **11**, 912083 (2023).
1153 2. Tan, O. L. & Fleming, J. S. Proliferating cell nuclear antigen immunoreactivity in the ovarian surface
1154 epithelium of mice of varying ages and total lifetime ovulation number following ovulation. *Biol. Reprod.*
1155 **71**, 1501–1507 (2004).
1156 3. Wang, J., Wang, D., Chu, K., Li, W. & Zeng, Y. A. Procr-expressing progenitor cells are responsible
1157 for murine ovulatory rupture repair of ovarian surface epithelium. *Nat. Commun.* **10**, 4966 (2019).
1158 4. Williams, C. J. & Erickson, G. F. Morphology and Physiology of the Ovary. in *Endotext* (eds.
1159 Feingold, K. R. et al.) (MDText.com, Inc., South Dartmouth (MA), 2012).
1160 5. Stickels, R. R. *et al.* Highly sensitive spatial transcriptomics at near-cellular resolution with Slide-
1161 seqV2. *Nat. Biotechnol.* **39**, 313–319 (2021).
1162 6. Rodriques, S. G. *et al.* Slide-seq: A scalable technology for measuring genome-wide expression at
1163 high spatial resolution. *Science* **363**, 1463–1467 (2019).
1164 7. Dunlop, C. E. & Anderson, R. A. The regulation and assessment of follicular growth. *Scand. J. Clin.*
1165 *Lab. Invest. Suppl.* **244**, 13–7; discussion 17 (2014).
1166 8. Shirasuna, K. & Iwata, H. Effect of aging on the female reproductive function. *Contracept. Reprod.*
1167 *Med.* **2**, 23 (2017).
1168 9. Amargant, F. *et al.* Ovarian stiffness increases with age in the mammalian ovary and depends on
1169 collagen and hyaluronan matrices. *Aging Cell* **19**, e13259 (2020).
1170 10. Mara, J. N. *et al.* Ovulation and ovarian wound healing are impaired with advanced reproductive age.
1171 *Aging* **12**, 9686–9713 (2020).
1172 11. Briley, S. M. *et al.* Reproductive age-associated fibrosis in the stroma of the mammalian ovary.
1173 *Reproduction* **152**, 245–260 (2016).
1174 12. Lliberos, C. *et al.* Evaluation of inflammation and follicle depletion during ovarian ageing in mice.
1175 *Sci. Rep.* **11**, 278 (2021).
1176 13. Wilkosz, P., Greggains, G. D., Tanbo, T. G. & Fedorcsak, P. Female reproductive decline is
1177 determined by remaining ovarian reserve and age. *PLoS One* **9**, e108343 (2014).
1178 14. LaVoie, H. A. Transcriptional control of genes mediating ovarian follicular growth, differentiation,
1179 and steroidogenesis in pigs. *Mol. Reprod. Dev.* **84**, 788–801 (2017).
1180 15. Vazakidou, P. *et al.* The profile of steroid hormones in human fetal and adult ovaries. *Reprod. Biol.*
1181 *Endocrinol.* **22**, 60 (2024).
1182 16. Richards, J. S., Ren, Y. A., Candelaria, N., Adams, J. E. & Rajkovic, A. Ovarian Follicular Theca Cell
1183 Recruitment, Differentiation, and Impact on Fertility: 2017 Update. *Endocr. Rev.* **39**, 1–20 (2018).

1184 17. Orisaka, M., Tajima, K., Tsang, B. K. & Kotsuji, F. Oocyte-granulosa-theca cell interactions during
1185 preantral follicular development. *J. Ovarian Res.* **2**, 9 (2009).
1186 18. McGee, E. A. & Hsueh, A. J. Initial and cyclic recruitment of ovarian follicles. *Endocr. Rev.* **21**, 200–
1187 214 (2000).
1188 19. Duncan, W. C., Cowen, G. M. & Illingworth, P. J. Steroidogenic enzyme expression in human corpora
1189 lutea in the presence and absence of exogenous human chorionic gonadotrophin (HCG). *Mol. Hum. Reprod.*
1190 **5**, 291–298 (1999).
1191 20. te Velde, E. R. & Pearson, P. L. The variability of female reproductive ageing. *Hum. Reprod. Update*
1192 **8**, 141–154 (2002).
1193 21. Esencan, E., Beroukhim, G. & Seifer, D. B. Age-related changes in Folliculogenesis and potential
1194 modifiers to improve fertility outcomes - A narrative review. *Reprod. Biol. Endocrinol.* **20**, 156 (2022).
1195 22. Zhang, Z., Schlamp, F., Huang, L., Clark, H. & Brayboy, L. Inflammaging is associated with shifted
1196 macrophage ontogeny and polarization in the aging mouse ovary. *J Reprod Fertil* **159**, 325–337 (2020).
1197 23. Jones, A. S. K. *et al.* Cellular atlas of the human ovary using morphologically guided spatial
1198 transcriptomics and single-cell sequencing. *Sci. Adv.* **10**, eadm7506 (2024).
1199 24. Alberico, H. C. & Woods, D. C. Role of granulosa cells in the aging ovarian landscape: A focus on
1200 mitochondrial and metabolic function. *Front. Physiol.* **12**, 800739 (2021).
1201 25. Cai, M. *et al.* Quercetin activates autophagy to protect rats ovarian granulosa cells from H2O2-induced
1202 aging and injury. *Eur. J. Pharmacol.* **966**, 176339 (2024).
1203 26. Zou, X. *et al.* Peroxiredoxin 4 deficiency induces accelerated ovarian aging through destroyed
1204 proteostasis in granulosa cells. *Biochim. Biophys. Acta Mol. Basis Dis.* **1870**, 167334 (2024).
1205 27. Dipali, S. S. *et al.* Proteomic quantification of native and ECM-enriched mouse ovaries reveals an age-
1206 dependent fibro-inflammatory signature. *Aging (Albany NY)* **15**, 10821–10855 (2023).
1207 28. Grosbois, J., Bailie, E. C., Kelsey, T. W., Anderson, R. A. & Telfer, E. E. Spatio-temporal remodelling
1208 of the composition and architecture of the human ovarian cortical extracellular matrix during in vitro
1209 culture. *Hum. Reprod.* **38**, 444–458 (2023).
1210 29. Pietroforte, S., Plough, M. & Amargant, F. Age-associated increased stiffness of the ovarian
1211 microenvironment impairs follicle development and oocyte quality and rapidly alters follicle gene
1212 expression. *bioRxivorg* 2024.06.09.598134 (2024) doi:10.1101/2024.06.09.598134.
1213 30. Hense, J. D. *et al.* The role of cellular senescence in ovarian aging. *NPJ Aging* **10**, 35 (2024).
1214 31. Isola, J. V. V. *et al.* Reproductive Ageing: Inflammation, immune cells, and cellular senescence in the
1215 aging ovary. *J Reprod Fertil* **168**, e230499 (2024).
1216 32. Trimmer, K. A. *et al.* Spatial single-cell sequencing of meiosis I arrested oocytes indicates acquisition
1217 of maternal transcripts from the soma. *Cell Rep.* **42**, (2023).

1218 33. Landry, D. A. *et al.* Metformin prevents age-associated ovarian fibrosis by modulating the immune
1219 landscape in female mice. *Sci. Adv.* **8**, eabq1475 (2022).
1220 34. Wang, Z., Liu, C.-Y., Zhao, Y. & Dean, J. FIGLA, LHX8 and SOHLH1 transcription factor networks
1221 regulate mouse oocyte growth and differentiation. *Nucleic Acids Res.* **48**, 3525–3541 (2020).
1222 35. Morris, M. E. *et al.* A single-cell atlas of the cycling murine ovary. *Elife* **11**, (2022).
1223 36. Ben Yaakov, T., Wasserman, T., Aknin, E. & Savir, Y. Single-cell analysis of the aged ovarian
1224 immune system reveals a shift towards adaptive immunity and attenuated cell function. *Elife* **12**, (2023).
1225 37. Isola, J. V. V. *et al.* A single-cell atlas of the aging mouse ovary. *Nat Aging* **4**, 145–162 (2024).
1226 38. Winkler, I. *et al.* The function and decline of the female reproductive tract at single-cell resolution.
1227 *bioRxiv* 2022.10.26.513823 (2022) doi:10.1101/2022.10.26.513823.
1228 39. Huang, R. *et al.* Single-cell and spatiotemporal profile of ovulation in the mouse ovary. *bioRxivorg*
1229 2024.05.20.594719 (2024).
1230 40. Bingel, A. S. & Schwartz, N. B. Timing of LH release and ovulation in the cyclic mouse. *J. Reprod.*
1231 *Fertil.* **19**, 223–229 (1969).
1232 41. Chen, Y.-Y. *et al.* Single-cell transcriptomics of staged oocytes and somatic cells reveal novel
1233 regulators of follicle activation. *J Reprod Fertil* **164**, 55–70 (2022).
1234 42. Binder, A. K., Winuthayanon, W., Hewitt, S. C., Couse, J. F. & Korach, K. S. Steroid receptors in the
1235 uterus and ovary. in *Knobil and Neill's Physiology of Reproduction* 1099–1193 (Elsevier, 2015).
1236 43. Jeppesen, J. V. *et al.* LH-receptor gene expression in human granulosa and cumulus cells from antral
1237 and preovulatory follicles. *J. Clin. Endocrinol. Metab.* **97**, E1524-31 (2012).
1238 44. Lee-Thacker, S. *et al.* Core Binding Factors are essential for ovulation, luteinization, and female
1239 fertility in mice. *Sci. Rep.* **10**, 9921 (2020).
1240 45. Romereim, S. M. *et al.* Gene expression profiling of bovine ovarian follicular and luteal cells provides
1241 insight into cellular identities and functions. *Mol. Cell. Endocrinol.* **439**, 379–394 (2017).
1242 46. Abedel-Majed, M. A., Romereim, S. M., Davis, J. S. & Cupp, A. S. Perturbations in lineage
1243 specification of granulosa and theca cells may alter corpus luteum formation and function. *Front.*
1244 *Endocrinol. (Lausanne)* **10**, 832 (2019).
1245 47. Hinsch, K. D. & Hinsch, E. The zona pellucida "receptors" ZP1, ZP2 and ZP3. *Andrologia* **31**, 320–
1246 322 (1999).
1247 48. Conti, M. & Kunitomi, C. A genome-wide perspective of the maternal mRNA translation program
1248 during oocyte development. *Semin. Cell Dev. Biol.* **154**, 88–98 (2024).
1249 49. Rajkovic, A., Pangas, S. A., Ballow, D., Suzumori, N. & Matzuk, M. M. NOBOX deficiency disrupts
1250 early folliculogenesis and oocyte-specific gene expression. *Science* **305**, 1157–1159 (2004).

1251 50. Kocabas, A. M. *et al.* The transcriptome of human oocytes. *Proc. Natl. Acad. Sci. U. S. A.* **103**, 14027–
1252 14032 (2006).
1253 51. Hamazaki, N. *et al.* Reconstitution of the oocyte transcriptional network with transcription factors.
1254 *Nature* **589**, 264–269 (2021).
1255 52. Jaffe, L. A. & Egbert, J. R. Regulation of mammalian oocyte meiosis by intercellular communication
1256 within the ovarian follicle. *Annu. Rev. Physiol.* **79**, 237–260 (2017).
1257 53. Manova, K., Nocka, K., Besmer, P. & Bachvarova, R. F. Gonadal expression of c-kit encoded at the
1258 W locus of the mouse. *Development* **110**, 1057–1069 (1990).
1259 54. Paulini, F. & Melo, E. O. The role of oocyte-secreted factors GDF9 and BMP15 in follicular
1260 development and oogenesis: GDF9 and BMP15 and the follicular development. *Reprod. Domest. Anim.* **46**,
1261 354–361 (2011).
1262 55. Tanaka, M., Hennebold, J. D., Macfarlane, J. & Adashi, E. Y. A mammalian oocyte-specific linker
1263 histone gene H1oo: homology with the genes for the oocyte-specific cleavage stage histone (cs-H1) of sea
1264 urchin and the B4/H1M histone of the frog. *Development* **128**, 655–664 (2001).
1265 56. Pangas, S. A. *et al.* Oogenesis requires germ cell-specific transcriptional regulators *Sohlh1* and *Lhx8*.
1266 *Proc. Natl. Acad. Sci. U. S. A.* **103**, 8090–8095 (2006).
1267 57. Hoodbhoy, T. *et al.* ZP2 and ZP3 traffic independently within oocytes prior to assembly into the
1268 extracellular zona pellucida. *Mol. Cell. Biol.* **26**, 7991–7998 (2006).
1269 58. Xie, J., Jin, Y. & Wang, G. The role of SCF ubiquitin-ligase complex at the beginning of life. *Reprod.*
1270 *Biol. Endocrinol.* **17**, 101 (2019).
1271 59. De La Chesnaye, E. *et al.* Fbxw15/Fbxo12J is an F-box protein-encoding gene selectively expressed
1272 in oocytes of the mouse ovary. *Biol. Reprod.* **78**, 714–725 (2008).
1273 60. Yoon, S.-J. *et al.* Role of Bcl2-like 10 (Bcl2l10) in regulating mouse oocyte maturation. *Biol. Reprod.*
1274 **81**, 497–506 (2009).
1275 61. Yu, C. *et al.* BTG4 is a meiotic cell cycle-coupled maternal-zygotic-transition licensing factor in
1276 oocytes. *Nat. Struct. Mol. Biol.* **23**, 387–394 (2016).
1277 62. Narducci, M. G. *et al.* TCL1 participates in early embryonic development and is overexpressed in
1278 human seminomas. *Proc. Natl. Acad. Sci. U. S. A.* **99**, 11712–11717 (2002).
1279 63. Haghverdi, L., Büttner, M., Wolf, F. A., Buettner, F. & Theis, F. J. Diffusion pseudotime robustly
1280 reconstructs lineage branching. *Nat. Methods* **13**, 845–848 (2016).
1281 64. Clément, F. *et al.* Growth kinetics of the granulosa cell population in ovarian follicles: an approach by
1282 mathematical modelling. *Cell Prolif.* **30**, 255–270 (1997).
1283 65. Kotliar, D. *et al.* Reproducible single cell annotation of programs underlying T-cell subsets, activation
1284 states, and functions. *bioRxivorg* 2024.05.03.592310 (2024).

1285 66. Pangas, S. A. *et al.* Intraovarian activins are required for female fertility. *Mol. Endocrinol.* **21**, 2458–
1286 2471 (2007).
1287 67. Klein, D. *et al.* Mapping cells through time and space with moscot. *bioRxiv* 2023.05.11.540374 (2023)
1288 doi:10.1101/2023.05.11.540374.
1289 68. Browaeys, R. *et al.* MultiNicheNet: a flexible framework for differential cell-cell communication
1290 analysis from multi-sample multi-condition single-cell transcriptomics data. *bioRxiv* 2023.06.13.544751
1291 (2023) doi:10.1101/2023.06.13.544751.
1292 69. Hofmann, S. M. *et al.* Adipocyte LDL receptor-related protein-1 expression modulates postprandial
1293 lipid transport and glucose homeostasis in mice. *J. Clin. Invest.* **117**, 3271–3282 (2007).
1294 70. Benitez-Amaro, A. *et al.* Low-density lipoprotein receptor-related protein 1 deficiency in
1295 cardiomyocytes reduces susceptibility to insulin resistance and obesity. *Metabolism* **106**, 154191 (2020).
1296 71. Qu, J. *et al.* Low-density lipoprotein receptor-related protein 1 (LRP1) is a novel receptor for
1297 apolipoprotein A4 (APOA4) in adipose tissue. *Sci. Rep.* **11**, 13289 (2021).
1298 72. Day, F. *et al.* Large-scale genome-wide meta-analysis of polycystic ovary syndrome suggests shared
1299 genetic architecture for different diagnosis criteria. *PLoS Genet.* **14**, e1007813 (2018).
1300 73. Cunningham, A. C. *et al.* Chronicling menstrual cycle patterns across the reproductive lifespan with
1301 real-world data. *Sci. Rep.* **14**, 10172 (2024).
1302 74. Peluso, J. J., Steger, R. W., Huang, H. & Meites, J. Pattern of follicular growth and steroidogenesis in
1303 the ovary of aging cycling rats. *Exp. Aging Res.* **5**, 319–333 (1979).
1304 75. Wang, H. *et al.* Rejuvenation of aged oocyte through exposure to young follicular microenvironment.
1305 *Nat. Aging* **4**, 1194–1210 (2024).
1306 76. Gill, A., Jamnongjit, M. & Hammes, S. R. Androgens promote maturation and signaling in mouse
1307 oocytes independent of transcription: a release of inhibition model for mammalian oocyte meiosis. *Mol.*
1308 *Endocrinol.* **18**, 97–104 (2004).
1309 77. Kawakami, S., Nansai, C. & Niimura, S. Inhibition of 20 α-Hydroxysteroid Dehydrogenase Activity
1310 in Mouse Oocyte by Human 20 α-HSD (AKR1C1) Inhibitor. *Journal of Biology and Today`s World* **9**, 1–
1311 4 (2020).
1312 78. Niimura, S. & Kawakami, S.-Y. Changes in the activities of hydroxysteroid dehydrogenases in mouse
1313 oocytes during meiotic maturation. *J. Reprod. Dev.* **49**, 451–456 (2003).
1314 79. Parkening, T. A., Collins, T. J. & Smith, E. R. Plasma and pituitary concentrations of LH, FSH, and
1315 prolactin in aging C57BL/6 mice at various times of the estrous cycle. *Neurobiol. Aging* **3**, 31–35 (1982).
1316 80. Nelson, J. F., Felicio, L. S., Osterburg, H. H. & Finch, C. E. Differential contributions of ovarian and
1317 extraovarian factors to age-related reductions in plasma estradiol and progesterone during the estrous cycle
1318 of C57BL/6J mice. *Endocrinology* **130**, 805–810 (1992).

1319 81. Hamatani, T. *et al.* Age-associated alteration of gene expression patterns in mouse oocytes. *Hum. Mol.*
1320 *Genet.* **13**, 2263–2278 (2004).
1321 82. Van Gorp, H., Kuchmiy, A., Van Hauwermeiren, F. & Lamkanfi, M. NOD-like receptors interfacing
1322 the immune and reproductive systems. *FEBS J.* **281**, 4568–4582 (2014).
1323 83. Kanzaki, S. *et al.* Involvement of Nlrp9a/b/c in mouse preimplantation development. *J Reprod Fertil*
1324 **160**, 181–191 (2020).
1325 84. Peng, H., Lin, X., Liu, F., Wang, C. & Zhang, W. NLRP9B protein is dispensable for oocyte
1326 maturation and early embryonic development in the mouse. *J. Reprod. Dev.* **61**, 559–564 (2015).
1327 85. Mondal, M. *et al.* Deciphering the luteal transcriptome: potential mechanisms mediating stage-specific
1328 luteolytic response of the corpus luteum to prostaglandin $F_2\alpha$. *Physiol. Genomics* **43**, 447–456 (2011).
1329 86. Smith, M. F., Ricke, W. A., Bakke, L. J., Dow, M. P. D. & Smith, G. W. Ovarian tissue remodeling:
1330 role of matrix metalloproteinases and their inhibitors. *Mol. Cell. Endocrinol.* **191**, 45–56 (2002).
1331 87. Faas, M. *et al.* The immune response during the luteal phase of the ovarian cycle: a Th2-type response?
1332 *Fertil. Steril.* **74**, 1008–1013 (2000).
1333 88. Poole, D. H. & Pate, J. L. Luteal microenvironment directs resident T lymphocyte function in cows.
1334 *Biol. Reprod.* **86**, 29 (2012).
1335 89. Wynn, T. A. & Vannella, K. M. Macrophages in tissue repair, regeneration, and fibrosis. *Immunity* **44**,
1336 450–462 (2016).
1337 90. Büttner, M., Ostner, J., Müller, C. L., Theis, F. J. & Schubert, B. scCODA is a Bayesian model for
1338 compositional single-cell data analysis. *Nat. Commun.* **12**, 6876 (2021).
1339 91. Wilkinson, H. N. *et al.* Tissue iron promotes wound repair via M2 macrophage polarization and the
1340 chemokine (C-C motif) ligands 17 and 22. *Am. J. Pathol.* **189**, 2196–2208 (2019).
1341 92. Swindell, W. R. *et al.* Meta-profiles of gene expression during aging: limited similarities between
1342 mouse and human and an unexpectedly decreased inflammatory signature. *PLoS One* **7**, e33204 (2012).
1343 93. Latorre, J. *et al.* Adipose tissue knockdown of lysozyme reduces local inflammation and improves
1344 adipogenesis in high-fat diet-fed mice. *Pharmacol. Res.* **166**, 105486 (2021).
1345 94. Saade, M., Araujo de Souza, G., Scavone, C. & Kinoshita, P. F. The role of GPNMB in inflammation.
1346 *Front. Immunol.* **12**, 674739 (2021).
1347 95. Ripoll, V. M., Irvine, K. M., Ravasi, T., Sweet, M. J. & Hume, D. A. Gpnmb is induced in macrophages
1348 by IFN-gamma and lipopolysaccharide and acts as a feedback regulator of proinflammatory responses. *J.*
1349 *Immunol.* **178**, 6557–6566 (2007).
1350 96. Lu, S. & Weiser-Evans, M. C. M. Lgals3-transitioned inflammatory smooth muscle cells: Major
1351 regulators of atherosclerosis progression and inflammatory cell recruitment. *Arteriosclerosis, thrombosis,*
1352 *and vascular biology* vol. 42 957–959 (2022).

1353 97. Huang, L. *et al.* Clinical significance of abnormal serum LGALS3BP expression in patients with
1354 idiopathic inflammatory myopathies. *J. Inflamm. Res.* **17**, 9697–9710 (2024).
1355 98. Foley, K. G., Pritchard, M. T. & Duncan, F. E. Macrophage-derived multinucleated giant cells:
1356 hallmarks of the aging ovary. *J Reprod Fertil* **161**, V5–V9 (2021).
1357 99. Kloc, M. *et al.* Giant Multinucleated Cells in Aging and Senescence-An Abridgement. *Biology* **11**,
1358 (2022).
1359 100. Baker, S. J. & Spears, N. The role of intra-ovarian interactions in the regulation of follicle dominance.
1360 *Hum. Reprod. Update* **5**, 153–165 (1999).
1361 101. Hyde, K. A. *et al.* Characterization of preantral follicle clustering and neighborhood patterns in the
1362 equine ovary. *PLoS One* **17**, e0275396 (2022).
1363 102. Robker, R. L. & Richards, J. S. Hormonal control of the cell cycle in ovarian cells: proliferation versus
1364 differentiation. *Biol. Reprod.* **59**, 476–482 (1998).
1365 103. Hatzirodos, N. *et al.* Transcriptome profiling of granulosa cells from bovine ovarian follicles during
1366 atresia. *BMC Genomics* **15**, 40 (2014).
1367 104. Irving-Rodgers, H. F., van Wezel, I. L., Mussard, M. L., Kinder, J. E. & Rodgers, R. J. Atresia
1368 revisited: two basic patterns of atresia of bovine antral follicles. *J Reprod Fertil* **122**, 761–775 (2001).
1369 105. Sen, A. *et al.* Androgens regulate ovarian follicular development by increasing follicle stimulating
1370 hormone receptor and microRNA-125b expression. *Proc. Natl. Acad. Sci. U. S. A.* **111**, 3008–3013 (2014).
1371 106. *Endocrine Facets of Ageing | Wiley*. (2008).
1372 107. Tang, M., Zhao, M. & Shi, Y. New insight into the role of macrophages in ovarian function and ovarian
1373 aging. *Front. Endocrinol. (Lausanne)* **14**, 1282658 (2023).
1374 108. Landau, S., Braw-Tal, R., Kaim, M., Bor, A. & Bruckental, I. Preovulatory follicular status and diet
1375 affect the insulin and glucose content of follicles in high-yielding dairy cows. *Anim. Reprod. Sci.* **64**, 181–
1376 197 (2000).
1377 109. Mantri, M., Zhang, H. H., Spanos, E., Ren, Y. A. & De Vlaminck, I. A spatiotemporal molecular atlas
1378 of the ovulating mouse ovary. *Proc. Natl. Acad. Sci. U. S. A.* **121**, e2317418121 (2024).
1379 110. McLean, A. C., Valenzuela, N., Fai, S. & Bennett, S. A. L. Performing vaginal lavage, crystal violet
1380 staining, and vaginal cytological evaluation for mouse estrous cycle staging identification. *J. Vis. Exp.*
1381 e4389 (2012).
1382 111. Byers, S. L., Wiles, M. V., Dunn, S. L. & Taft, R. A. Mouse estrous cycle identification tool and
1383 images. *PLoS One* **7**, e35538 (2012).
1384 112. Ajayi, A. F. & Akhigbe, R. E. Staging of the estrous cycle and induction of estrus in experimental
1385 rodents: an update. *Fertil Res Pract* **6**, 5 (2020).

1386 113. Bertolin, K. & Murphy, B. D. 7 - Reproductive Tract Changes During the Mouse Estrous Cycle. in
1387 *The Guide to Investigation of Mouse Pregnancy* (eds. Croy, B. A., Yamada, A. T., DeMayo, F. J. &
1388 Adamson, S. L.) 85–94 (Academic Press, Boston, 2014).
1389 114. Zheng, G. X. Y. *et al.* Massively parallel digital transcriptional profiling of single cells. *Nat. Commun.*
1390 **8**, 14049 (2017).
1391 115. Dobin, A. *et al.* STAR: ultrafast universal RNA-seq aligner. *Bioinformatics* **29**, 15–21 (2013).
1392 116. Wolf, F. A., Angerer, P. & Theis, F. J. SCANPY: large-scale single-cell gene expression data analysis.
1393 *Genome Biol.* **19**, 15 (2018).
1394 117. Korsunsky, I. *et al.* Fast, sensitive and accurate integration of single-cell data with Harmony. *Nat.*
1395 *Methods* **16**, 1289–1296 (2019).
1396 118. McInnes, L., Healy, J. & Melville, J. UMAP: Uniform Manifold Approximation and Projection for
1397 Dimension Reduction. *arXiv [stat.ML]* (2018).
1398 119. Meinsohn, M.-C. *et al.* Single-cell sequencing reveals suppressive transcriptional programs regulated
1399 by MIS/AMH in neonatal ovaries. *Proc. Natl. Acad. Sci. U. S. A.* **118**, (2021).
1400 120. Kapfhamer, J., Waite, C. & Ascoli, M. The Gαq/11-provoked induction of Akr1c18 in murine luteal
1401 cells is mediated by phospholipase C. *Mol. Cell. Endocrinol.* **470**, 179–187 (2018).
1402 121. Le Goascogne, C. *et al.* Immunoreactive cytochrome P-450(17 alpha) in rat and guinea-pig gonads,
1403 adrenal glands and brain. *J. Reprod. Fertil.* **93**, 609–622 (1991).
1404 122. Luo, W. & Wiltbank, M. C. Distinct regulation by steroids of messenger RNAs for FSHR and
1405 CYP19A1 in bovine granulosa cells. *Biol. Reprod.* **75**, 217–225 (2006).
1406 123. Yung, Y. *et al.* Localization of luteinizing hormone receptor protein in the human ovary. *Mol. Hum.*
1407 *Reprod.* **20**, 844–849 (2014).
1408 124. Traag, V. A., Waltman, L. & van Eck, N. J. From Louvain to Leiden: guaranteeing well-connected
1409 communities. *Sci. Rep.* **9**, 5233 (2019).
1410 125. Kotliar, D. *et al.* Identifying gene expression programs of cell-type identity and cellular activity with
1411 single-cell RNA-Seq. *Elife* **8**, (2019).
1412 126. Buitinck, L. *et al.* API design for machine learning software: experiences from the scikit-learn project.
1413 *arXiv [cs.LG]* (2013).
1414 127. Niu, W. & Spradling, A. C. Two distinct pathways of pregranulosa cell differentiation support follicle
1415 formation in the mouse ovary. *Proc. Natl. Acad. Sci. U. S. A.* **117**, 20015–20026 (2020).
1416 128. Zhang, Y. *et al.* Transcriptome Landscape of Human Folliculogenesis Reveals Oocyte and Granulosa
1417 Cell Interactions. *Mol. Cell* **72**, 1021-1034.e4 (2018).
1418 129. Tirosh, I. *et al.* Dissecting the multicellular ecosystem of metastatic melanoma by single-cell RNA-
1419 seq. *Science* **352**, 189–196 (2016).

130. Palla, G. *et al.* Squidpy: a scalable framework for spatial omics analysis. *Nat. Methods* **19**, 171–178 (2022).

Figure 1

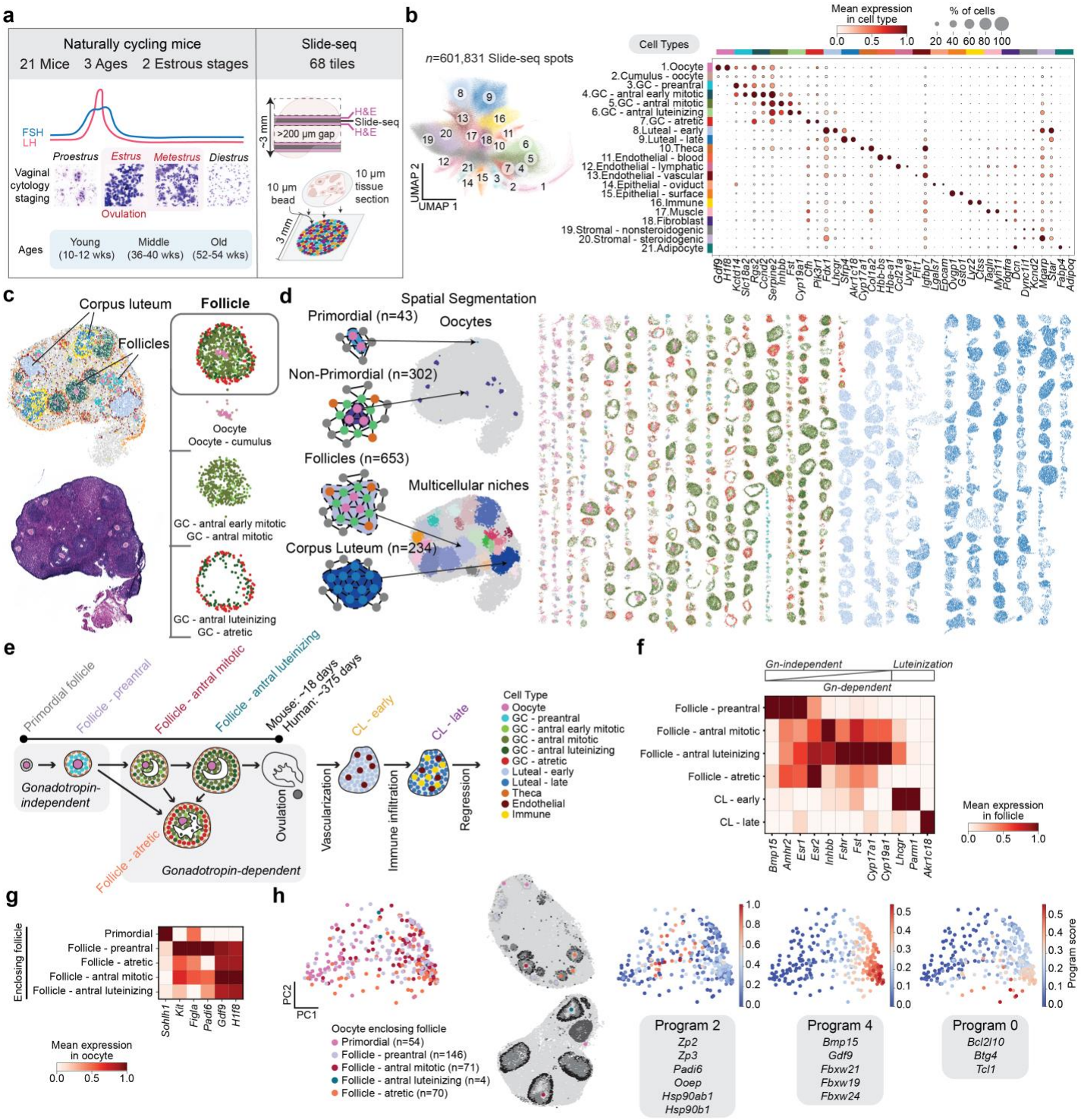
a
Naturally cycling mice
21 Mice 3 Ages 2 Estrous stages
Slide-seq
68 tiles
FSH
LH
Proestrus
Estrus
Metestrus
Diestrus
Vaginal cytology staging
Ovulation
Ages
Young (10-12 wks)
Middle (36-40 wks)
Old (52-54 wks)
~3 mm
>200 µm gap
H&E
Slide-seq
H&E
10 µm bead
10 µm tissue section
b
n=601,831 Slide-seq spots
UMAP 2
UMAP 1
Cell Types
Mean expression in cell type
% of cells
1.Oocyte
2.Cumulus - oocyte
3.GC - preantral
4.GC - antral early mitotic
5.GC - antral mitotic
6.GC - antral luteinizing
7.GC - atretic
8.Luteal - early
9.Luteal - late
10.Theca
11.Endothelial - blood
12.Endothelial - lymphatic
13.Endothelial - vascular
14.Epithelial - oviduct
15.Epithelial - surface
16.Immune
17.Muscle
18.Fibroblast
19.Stromal - nonsteroidogenic
20.Stromal - steroidogenic
21.Adipocyte
c
Corpus luteum
Follicles
Follicle
Oocyte
Oocyte - cumulus
GC - antral early mitotic
GC - antral mitotic
GC - antral luteinizing
GC - atretic
d
Spatial Segmentation
Primordial (n=43)
Oocytes
Non-Primordial (n=302)
Follicles (n=653)
Multicellular niches
Corpus Luteum (n=234)
e
Primordial follicle
Follicle - preantral
Follicle - antral mitotic
Follicle - antral luteinizing
Mouse: ~18 days
Human: ~375 days
Gonadotropin-independent
Follicle - atretic
Gonadotropin-dependent
Ovulation
CL - early
CL - late
Vascularization
Immune infiltration
Regression
Cell Type
Oocyte
GC - preantral
GC - antral early mitotic
GC - antral mitotic
GC - antral luteinizing
GC - atretic
Luteal - early
Luteal - late
Theca
Endothelial
Immune
f
Gn-independent
Luteinization
Gn-dependent
Follicle - preantral
Follicle - antral mitotic
Follicle - antral luteinizing
Follicle - atretic
CL - early
CL - late
Bmp15
Amhr2
Esr1
Esr2
Inhbb
Fshr
Fst
Cyp17a1
Cyp19a1
Lhcgr
Parm1
Akr1c18
Mean expression in follicle
g
Enclosing follicle
Primordial
Follicle - preantral
Follicle - atretic
Follicle - antral mitotic
Follicle - antral luteinizing
Sohlh1
Kit
Figla
Padi6
Gdf9
H1f8
Mean expression in oocyte
h
PC2
PC1
Oocyte enclosing follicle
Primordial (n=54)
Follicle - preantral (n=146)
Follicle - antral mitotic (n=71)
Follicle - antral luteinizing (n=4)
Follicle - atretic (n=70)
Program 2
Zp2
Zp3
Padi6
Ooep
Hsp90ab1
Hsp90b1
Program 4
Bmp15
Gdf9
Fbxw21
Fbxw19
Fbxw24
Program 0
Bcl2l10
Btg4
Tcl1
Program score

Figure 2

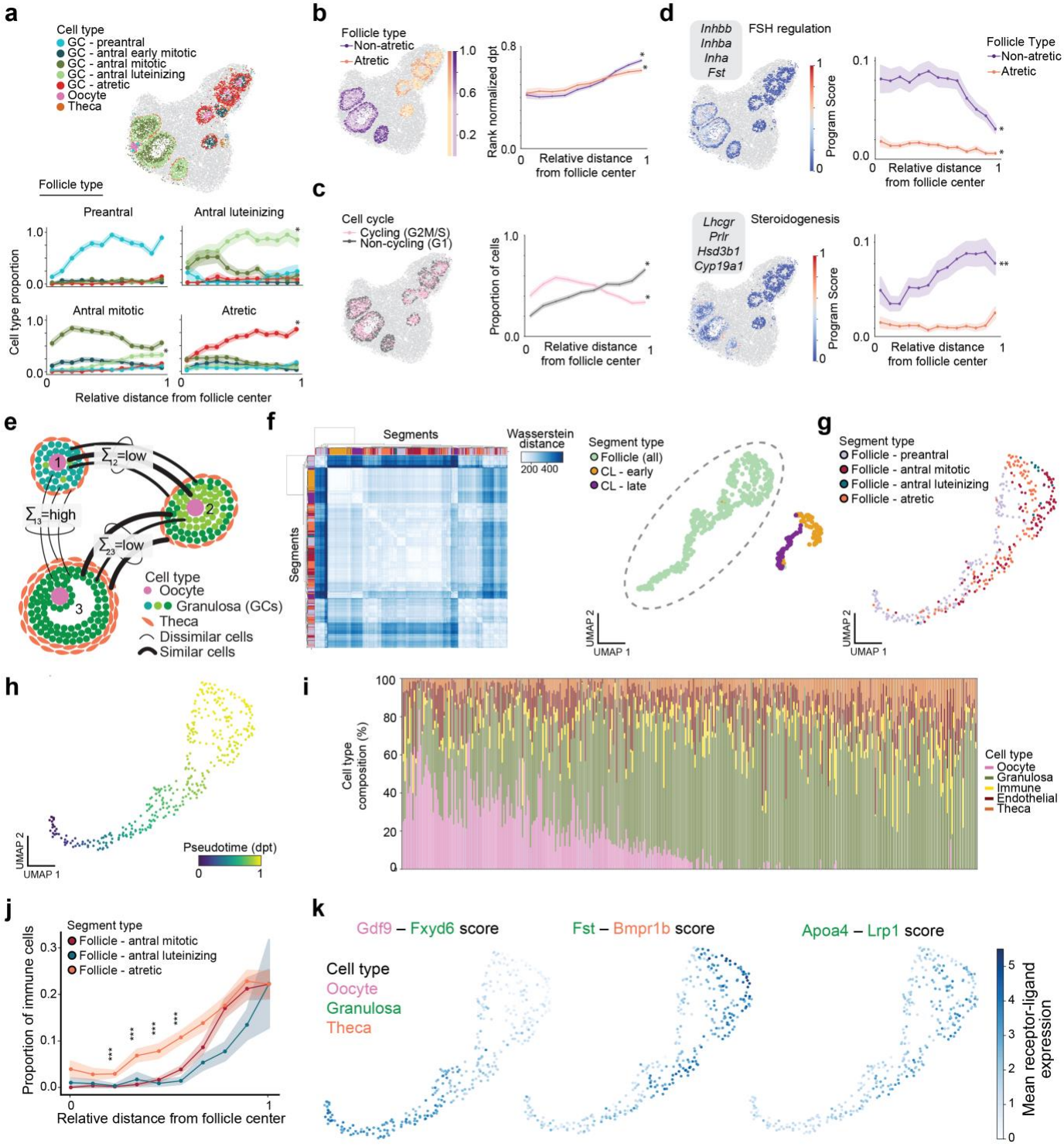
a
Cell type
GC - preantral
GC - antral early mitotic
GC - antral mitotic
GC - antral luteinizing
GC - atretic
Oocyte
Theca
Follicle type
Preantral
Antral luteinizing
Antral mitotic
Atretic
Cell type proportion
Relative distance from follicle center
b
Follicle type
Non-atretic
Atretic
Rank normalized dpt
Relative distance from follicle center
c
Cell cycle
Cycling (G2M/S)
Non-cycling (G1)
Proportion of cells
Relative distance from follicle center
d
Inhbb
Inhba
Inha
Fst
FSH regulation
Program Score
Follicle Type
Non-atretic
Atretic
Relative distance from follicle center
Lhcgr
Prlr
Hsd3b1
Cyp19a1
Steroidogenesis
Program Score
Relative distance from follicle center
e
Σ12=low
Σ13=high
Σ23=low
Cell type
Oocyte
Granulosa (GCs)
Theca
Dissimilar cells
Similar cells
f
Segments
Wasserstein distance
200 400
Segments
Segment type
Follicle (all)
CL - early
CL - late
UMAP 2
UMAP 1
g
Segment type
Follicle - preantral
Follicle - antral mitotic
Follicle - antral luteinizing
Follicle - atretic
UMAP 2
UMAP 1
h
UMAP 2
UMAP 1
Pseudotime (dpt)
i
Cell type composition (%)
Cell type
Oocyte
Granulosa
Immune
Endothelial
Theca
j
Segment type
Follicle - antral mitotic
Follicle - antral luteinizing
Follicle - atretic
Proportion of immune cells
Relative distance from follicle center
k
Gdf9 – Fxyd6 score
Fst – Bmpr1b score
Apoa4 – Lrp1 score
Cell type
Oocyte
Granulosa
Theca
Mean receptor-ligand expression

Figure 3

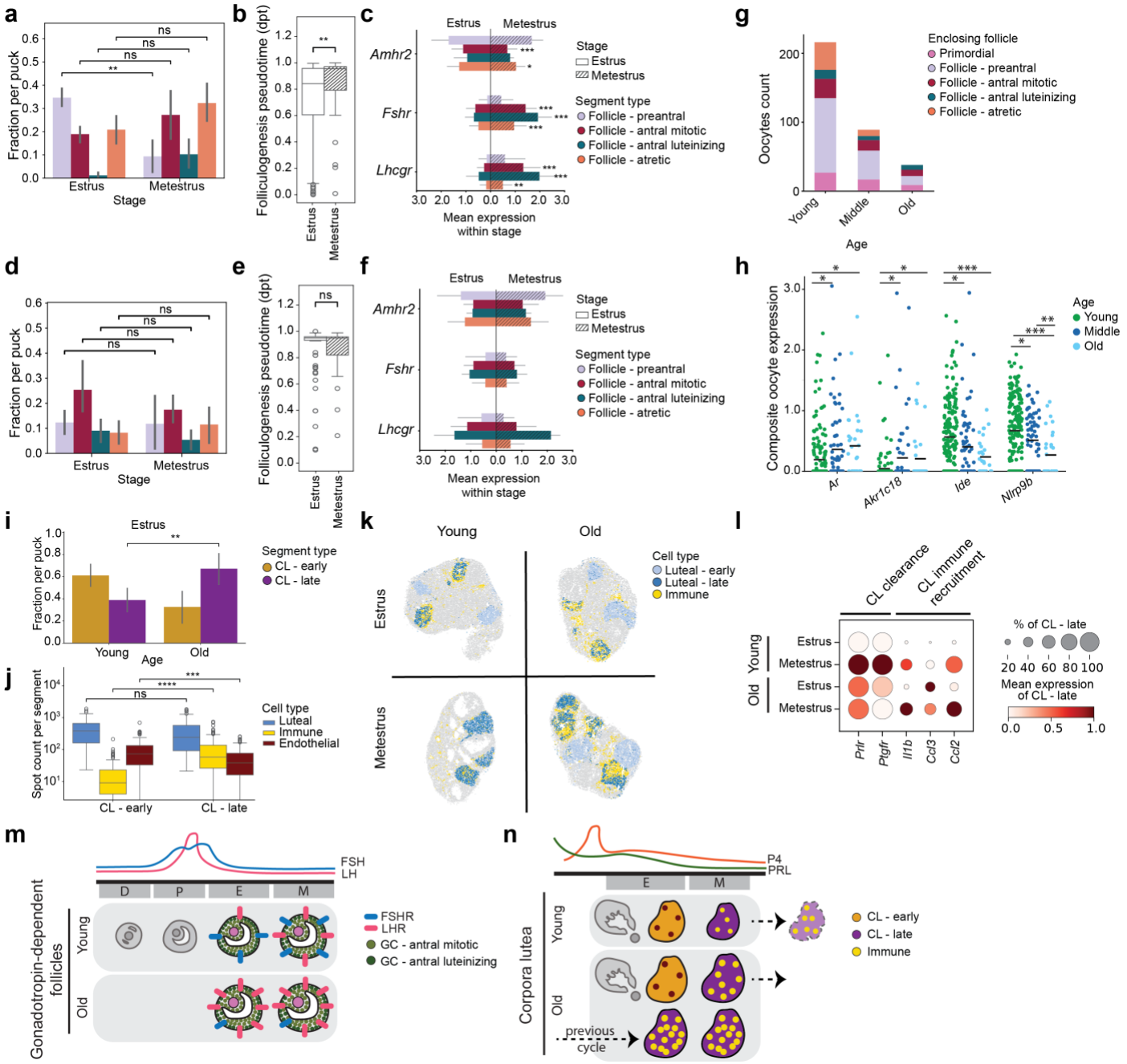
a
Fraction per puck
Estrus
Metestrus
Stage
ns
**
b
Folliculogenesis pseudotime (dpt)
c
Estrus
Metestrus
Amhr2
Fshr
Lhcgr
Mean expression within stage
Stage
Estrus
Metestrus
Segment type
Follicle - preantral
Follicle - antral mitotic
Follicle - antral luteinizing
Follicle - atretic
g
Oocytes count
Young
Middle
Old
Age
Enclosing follicle
Primordial
Follicle - preantral
Follicle - antral mitotic
Follicle - antral luteinizing
Follicle - atretic
d
e
f
h
Composite oocyte expression
Ar
Akr1c18
Ide
Nlrp9b
Age
Young
Middle
Old
i
Estrus
Fraction per puck
Young
Old
Age
Segment type
CL - early
CL - late
j
Spot count per segment
CL - early
CL - late
Cell type
Luteal
Immune
Endothelial
k
Young
Old
Estrus
Metestrus
Cell type
Luteal - early
Luteal - late
Immune
l
CL clearance
CL immune recruitment
Young
Old
Estrus
Metestrus
Prlr
Ptgfr
Il1b
Ccl3
Ccl2
% of CL - late
Mean expression of CL - late
m
FSH
LH
D
P
E
M
Gonadotropin-dependent follicles
Young
Old
FSHR
LHR
GC - antral mitotic
GC - antral luteinizing
n
P4
PRL
E
M
Corpora lutea
Young
Old
previous cycle
CL - early
CL - late
Immune

Figure 4

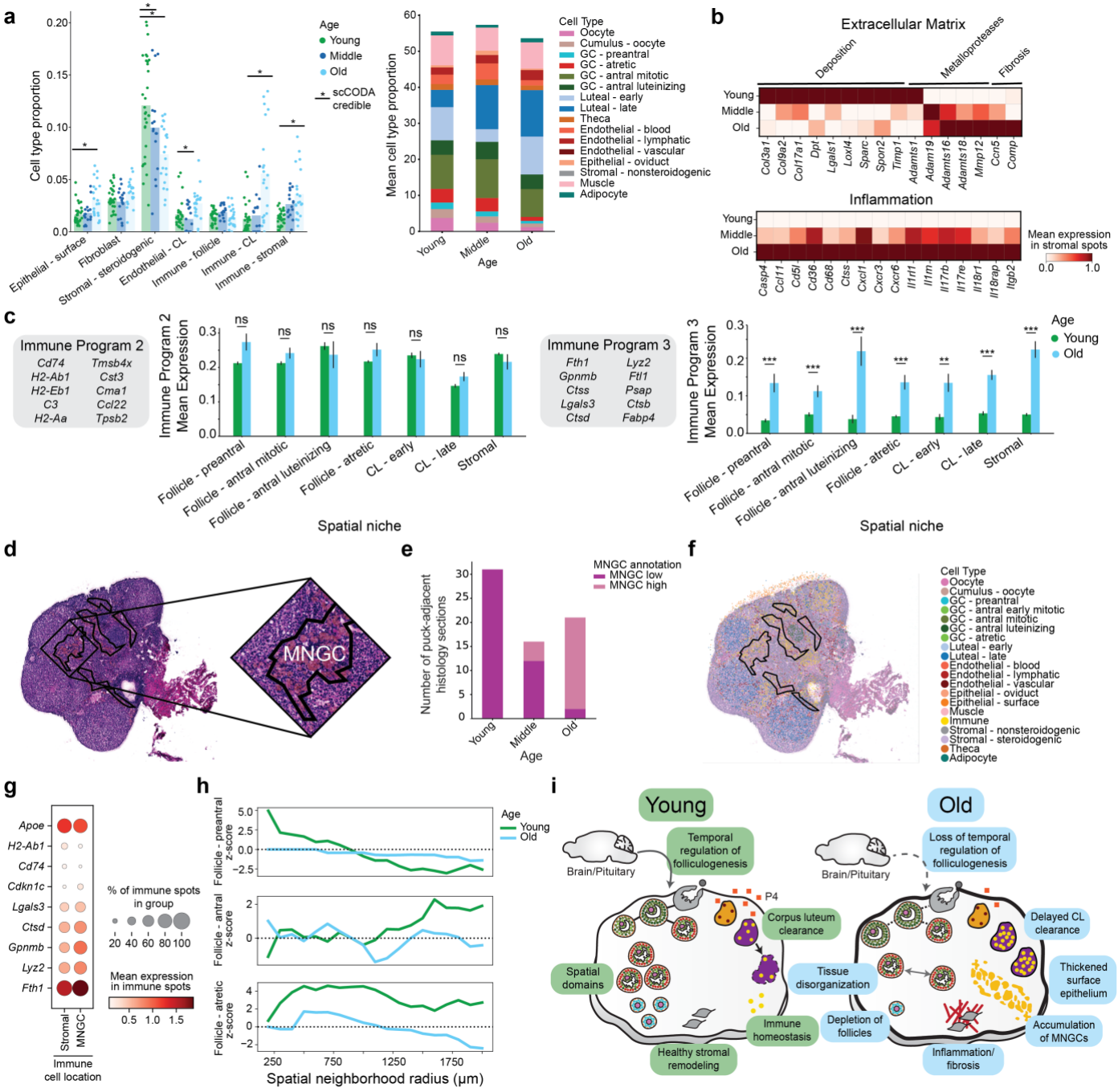
a
Cell type proportion
Age
Young
Middle
Old
scCODA credible
Epithelial - surface
Fibroblast
Stromal - steroidogenic
Endothelial - CL
Immune - follicle
Immune - CL
Immune - stromal
Mean cell type proportion
Cell Type
Oocyte
Cumulus - oocyte
GC - preantral
GC - atretic
GC - antral mitotic
GC - antral luteinizing
Luteal - early
Luteal - late
Theca
Endothelial - blood
Endothelial - lymphatic
Endothelial - vascular
Epithelial - oviduct
Stromal - nonsteroidogenic
Muscle
Adipocyte
b
Extracellular Matrix
Deposition
Metalloproteases
Fibrosis
Inflammation
Mean expression in stromal spots
c
Immune Program 2
Cd74 Tmsb4x
H2-Ab1 Cst3
H2-Eb1 Cma1
C3 Ccl22
H2-Aa Tpsb2
Immune Program 2 Mean Expression
Immune Program 3
Fth1 Lyz2
Gpnmb Ftl1
Ctss Psap
Lgals3 Ctsb
Ctsd Fabp4
Immune Program 3 Mean Expression
Follicle - preantral
Follicle - antral mitotic
Follicle - antral luteinizing
Follicle - atretic
CL - early
CL - late
Stromal
Spatial niche
d
MNGC
e
MNGC annotation
MNGC low
MNGC high
Number of puck-adjacent histology sections
f
g
% of immune spots in group
Mean expression in immune spots
Immune cell location
h
Follicle - preantral z-score
Follicle - antral z-score
Follicle - atretic z-score
Spatial neighborhood radius (μm)
i
Young
Old
Brain/Pituitary
Temporal regulation of folliculogenesis
Loss of temporal regulation of folliculogenesis
P4
Corpus luteum clearance
Delayed CL clearance
Spatial domains
Tissue disorganization
Thickened surface epithelium
Immune homeostasis
Depletion of follicles
Accumulation of MNGCs
Healthy stromal remodeling
Inflammation/ fibrosis

Extended Data Fig. 1

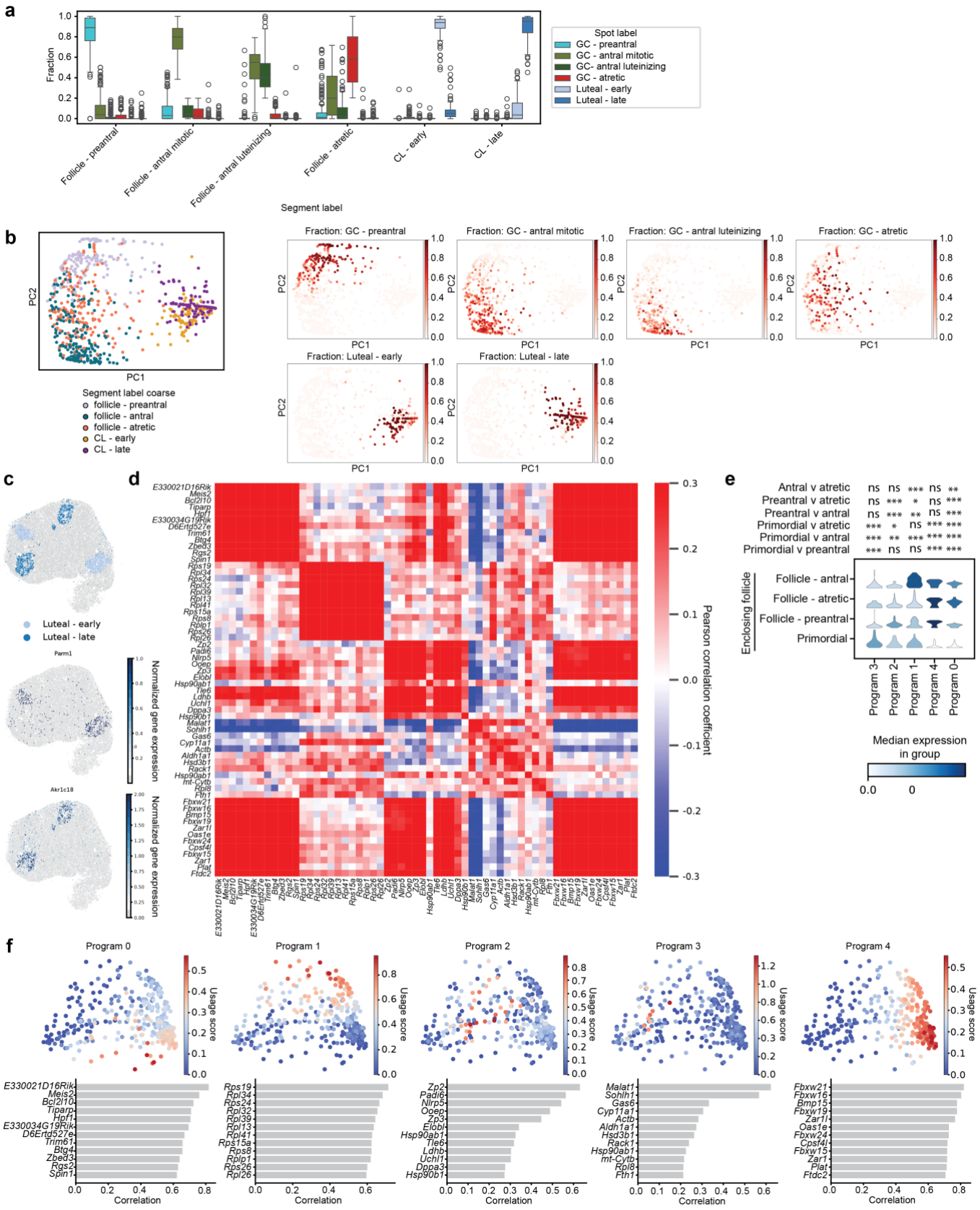

Extended Data Fig. 2

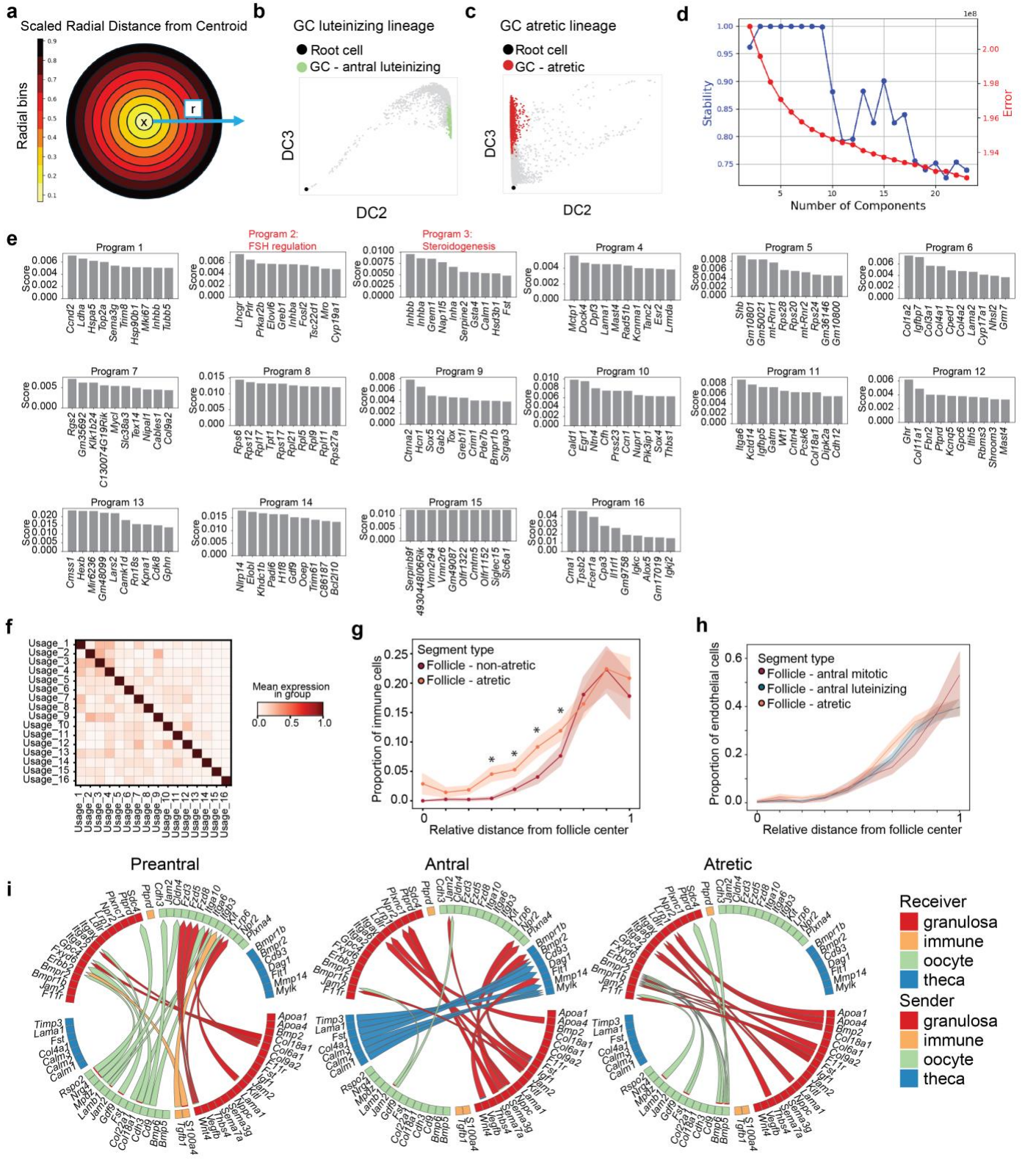

Extended Data Fig. 3

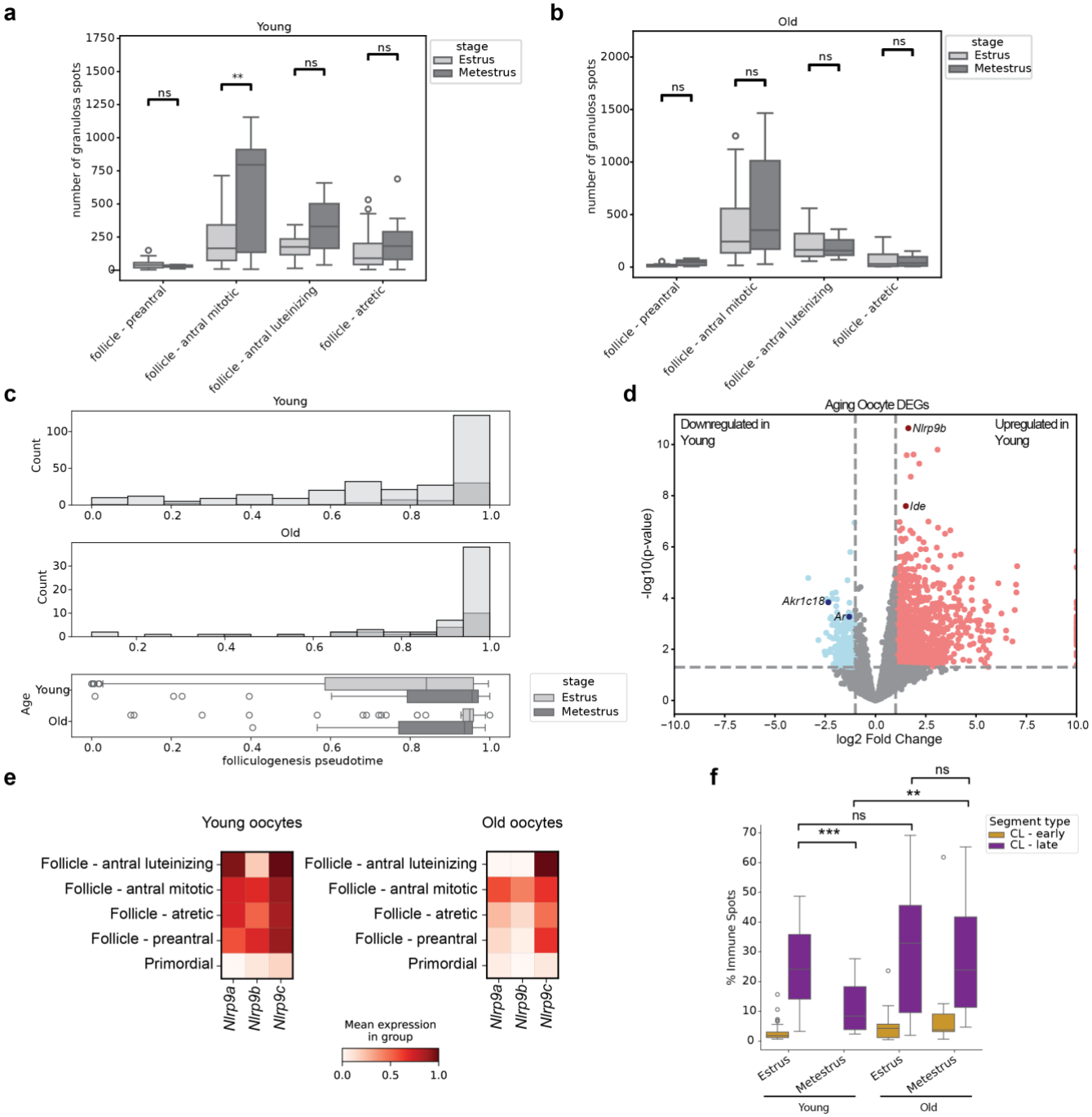

Extended Data Fig. 4

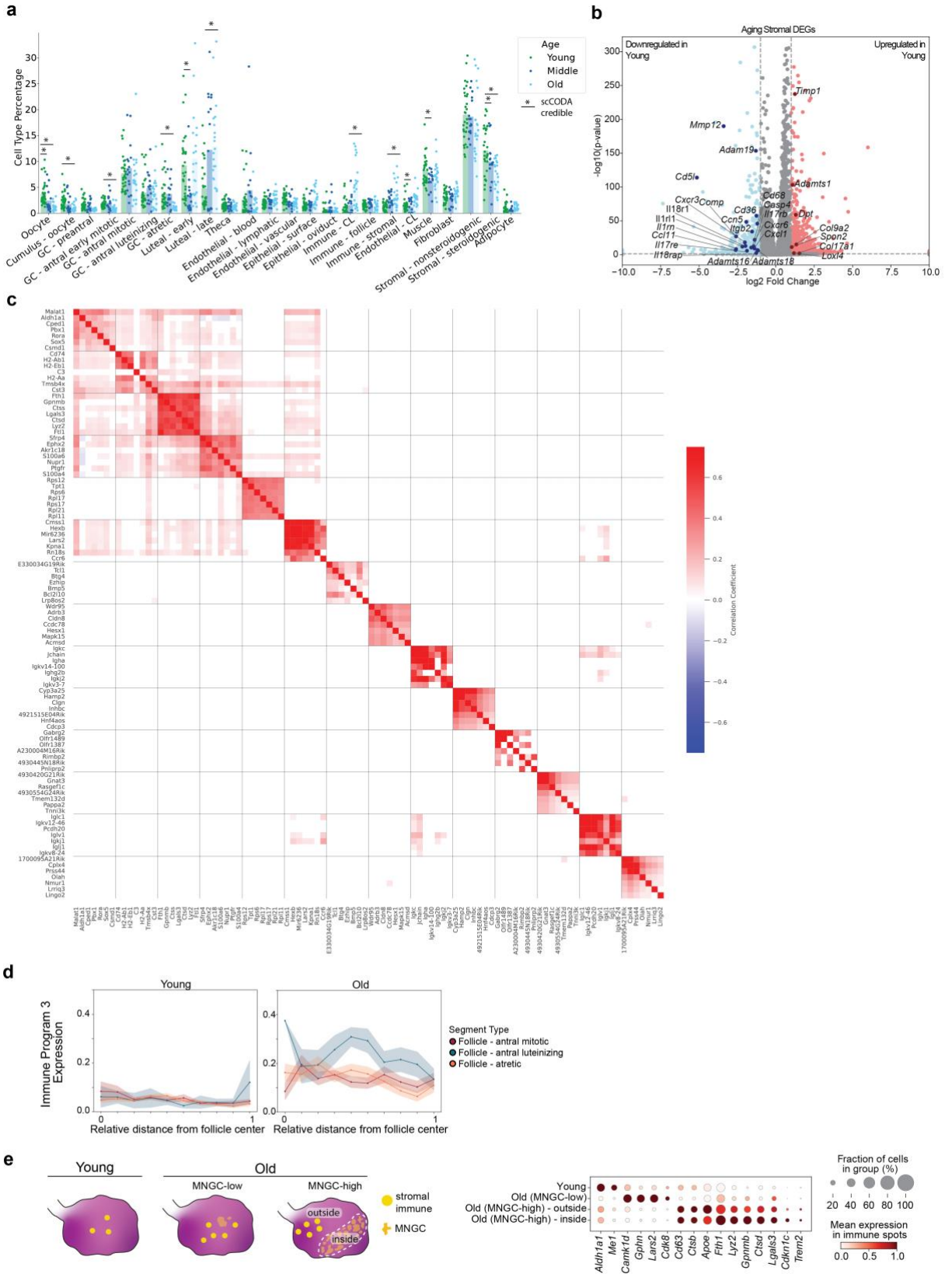
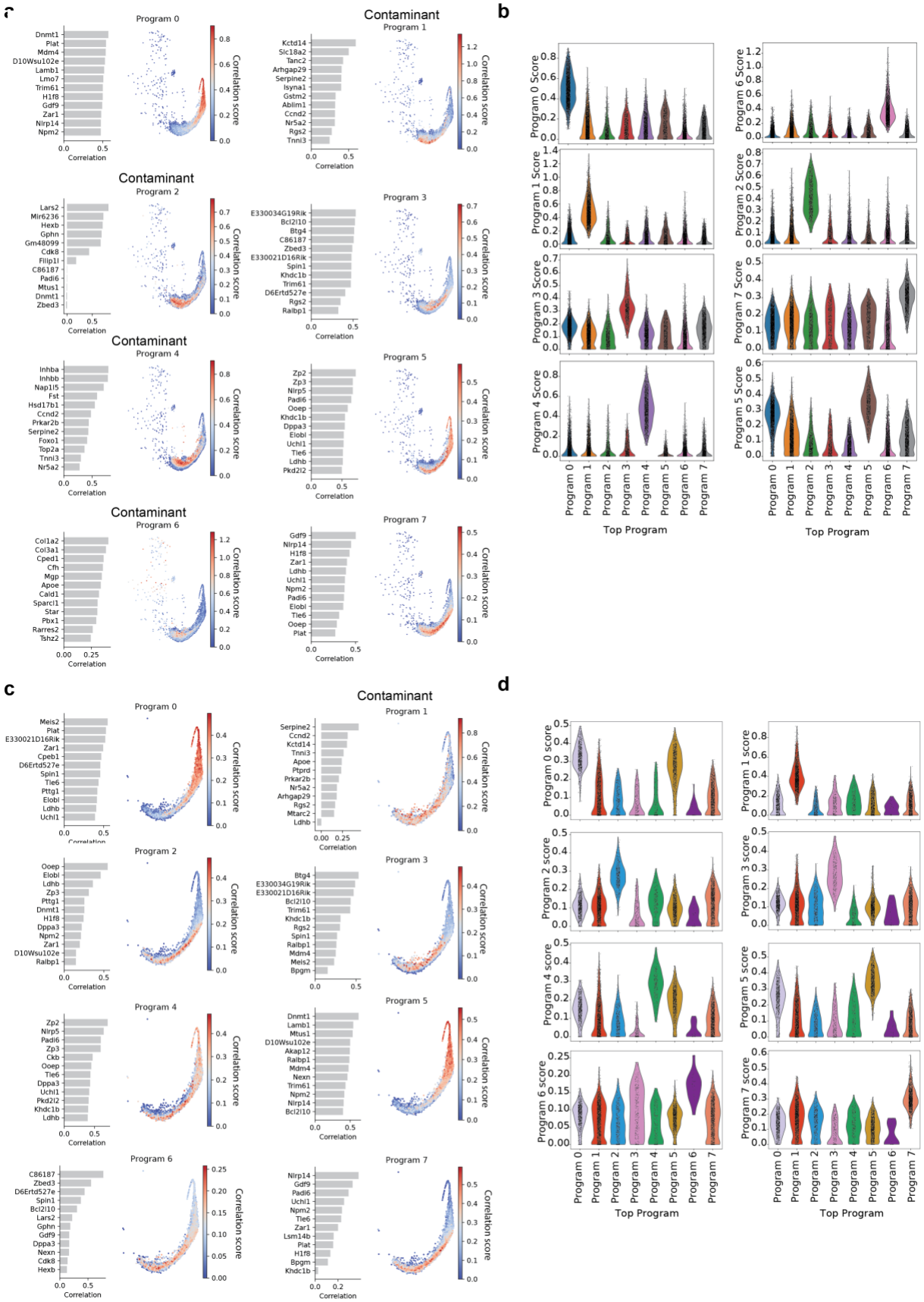
Extended Data Fig. 5